REVIEW

Electrocatalysis

Energy & Environmental Materials WILEY

Two-Dimensional Metallophthalocyanine Nanomaterials for Electrocatalytic Energy Conversion

Xinqi Wang, Shaohui Sun, Jiahao Yao, Hao Wan, Renzhi Ma, and Wei Ma**

Growing energy demand drives the rapid development of clean and reliable energy sources. In the past years, the exploration of novel materials with considerable efficiency and durability has drawn attention in the area of electrochemical energy conversion. Transition metal macrocyclic metallophthalocyanines (MPcs)-based catalysts with a peculiar 2D constitution have emerged with a promising future account of their highly structural tailorability and molecular functionality which greatly extend their functionalities as electrocatalytic materials for energy conversion. This review summarizes the systematic engineering of synthesis of MPcs and their analogs in detail, and mostly pays attention to the frontier research of MPc-based high-performance catalysts toward different electrocatalytic processes concerning hydrogen, oxygen, water, carbon dioxide, and nitrogen, with a particular focus on discussing the interrelationship between the electrocatalytic activity and component/structure, as well as functional applications of MPcs. Finally, we give the gaps that need to be addressed after much thought.

1. Introduction

Over recent years, increasingly prominent environmental issues have drawn much attention because of the tremendous challenge of rapidly climbing trends in energy consumption.[1] At present, the conversion and utilization of sustainable energy through (photo)electrochemical devices (or systems) are expected to replace the position of traditional fossil fuels in the energy industry chain.[2,3] In this aspect, clean energy conversion technologies play a key role in economic development. To effectively accelerate these energy conversions, high-efficiency electrocatalysts are extensively adopted.

Nowadays, although precious metal-based catalysts (e.g., Pt/C, Ir/C, RuO_2) are still popular in large-scale commercial markets, their extremely stiff price and scarce reserves limit the large-scale applications of electrocatalytic devices/systems.[4] It is therefore of great importance to develop cheap and viable alternatives.[5] Nanostructures based on transition metal elements (Fe, Co, and Ni) have been endowed with great promise as the combined merits of unique 3d electronic configuration, low cost, and redox properties. Among them, M–N_4–C materials with both specific macrocyclic structures and well-defined catalytically active units represent a class of molecular-scale catalysts, such as metallophthalocyanines (MPcs) and metalloporphyrins (MPys), where M represents non-noble transition metal elements with particular 3d electron configurations located on the center of planar organic molecules.[6]

Especially, the MPc-based materials demonstrated a significant contribution in the field of electrocatalytic energy conversion (**Figure 1**), however, moderate catalyst activity and performance were generally obtained, partly due to their insulating nature.[7–10] In addition, almost all alternative energy technologies are limited by the intrinsic properties of current materials. For example, the strong π–π stacking interaction of MPcs resulted from the large π-conjugated system made micromolecules easy to agglomerate, which not only restricted the contact with reactants but also reduced the electron transfer ability, diminishing the electrocatalytic activity.[11,12] Therefore, supporting carriers were introduced to not only significantly improve the electrical conductivity of the material via the modulation of the surface properties of MPcs but also retard the agglomerate phenomenon, enhancing the electrocatalytic processes.[13,14] On the other hand, MPc-based metal–organic frameworks (MOFs) and covalent organic frameworks (COFs), a new type of crystalline porous layered materials that integrate the catalytically active molecules via precise linkages, have gradually become potential heterogeneous candidates for electrocatalysis. In addition, during long-term electrochemical cycling, ion delocalization/clustering may occur and generate lattice stress within the electrode material, leading to structural degradation and crushing in the frameworks.[15] Hence, it is expected to design high-efficiency and robust electrocatalysts to meet the practical applications, which also lays a foundation for electrocatalysis theory.[16]

Therefore, the electrical conductivity of the material should be fully considered to improve the electrocatalytic performance. Up to date, there are some excellent review articles on the progress of MPc-based electrocatalysts mostly focusing on MPc molecules and/or single molecular units compounded with a carbon-based substrate for energy conversion, but the metal macrocyclic structures with fascinating conjugation effects have been rarely summarized.[17–21] Besides, the insulating nature of individual MPc molecular units severely influences the electrocatalytic performance, and needs to be effectively alleviated. Thus, it is of great value to review the latest MPc materials in the

X. Wang, Prof. S. Sun, J. Yao, Dr. H. Wan, Dr. W. Ma
School of Chemical Engineering and Zhongyuan Critical Metals Laboratory, Zhengzhou University, Zhengzhou 450001, China
E-mail: wanhao@zzu.edu.cn
E-mail: mawei@zzu.edu.cn
Prof. R. Ma
Research Center for Materials Nanoarchitectonics (MANA), National Institute for Materials Science (NIMS), Namiki 1-1, Tsukuba, Ibaraki 305-0044, Japan
The ORCID identification number(s) for the author(s) of this article can be found under https://doi.org/10.1002/eem2.12709.

DOI: 10.1002/eem2.12709

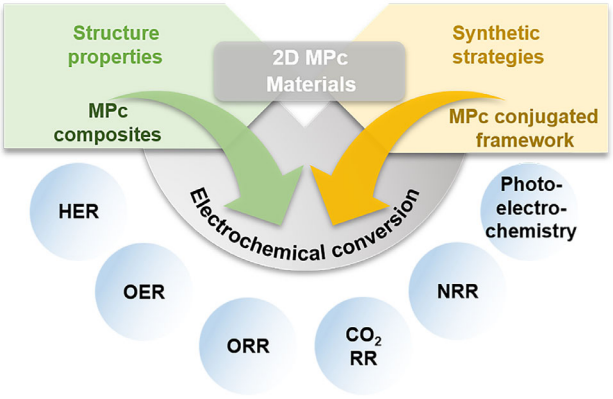

Figure 1. Schematic diagram of MPc materials applied on energy conversion application.

construction of 2D-conjugated macrocyclic frameworks for available applications.

In this respect, we give an overview of the research advances of MPcs, with an emphasis placed on MPc-based conjugated porous materials. Typically, the catalytic activity around active sites in MPc materials can be optimized through unique electronic configuration regulation. Unlike the reported reviews, this article summarizes the structural adjustment and performance improvement of representative conjugated MPcs for the first time. In particular, two methods including support loading and macrocyclic conjugation strategies, widely adopted to enhance the electrocatalytic performance, have been introduced in detail. First, we summarize the structure features and basic physicochemical properties of MPcs. Then, the general synthetic techniques of MPc catalysts are described for supported metal phthalocyanines and conjugated metal phthalocyanines. Subsequently, catalytic applications of MPc-based electrocatalysts as electrode materials in various electrochemical reactions are mainly discussed, such as hydrogen evolution reaction (HER), oxygen evolution reaction (OER), oxygen reduction reaction (ORR), carbon dioxide reduction reaction (CO_2RR), and nitrogen reduction reaction (NRR). Meanwhile, with rational composition optimization and structure design, the electronic configuration on the nanostructures is effectively modulated to achieve the most suitable adsorption strength of intermediates, and the underlying structure–activity relationship of the electrocatalysts is revealed. At last, development challenges, as well as outlooks of MPcs materials, are proposed. It is expected that this review may provide an in-depth reflection of the importance of electronic modulation on the MPc-based catalysts and offer significant inspiration for enhanced catalytic performance by microstructure engineering in molecular catalysis platforms.

2. Structure and Basic Physicochemical Properties of Metallophthalocyanines

In 1907, Braun and Tcherniac obtained a certain amount of blue precipitates and accidentally discovered the first nuclear-free phthalocyanine compound (H_2Pc).[22,23] As shown in **Figure 2**a, MPcs as derivatives of MPys composed of four isoindoline units with 18 π–electrons and its molecular structures are similar to the porphyrins, a kind of active substance existing in the biological world.[24–26] The difference is that

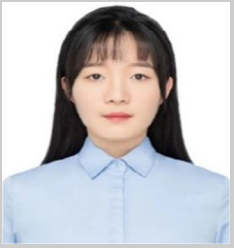

Xinqi Wang is a graduate student at the School of Chemical Engineering, Zhengzhou University, China, having received her bachelor's degree in chemical engineering and technology from the Lanzhou Jiaotong University, China in 2021. Her research focuses on the development of efficient electrocatalysts for energy conversion.

Shaohui Sun received his bachelor's and master's degrees in the Department of Chemistry from the Fudan University, China. In 2005, he received PhD degree in the School of Chemical Engineering from the Zhengzhou University, China. Since 2006, he has been working at the Zhengzhou University, China, where he is now a professor at the Advanced Functional Material Manufacturing Ministry of Education Engineering Center, School of Chemical Engineering. His research focuses on the development and theoretical investigation of advanced nanocatalysts for efficient clean energy conversion.

Hao Wan is an assistant professor of the School of Chemical Engineering and Zhongyuan Critical Metals Laboratory at the Zhengzhou University. He received his BSs (2013) and PhD (2019) from the Central South University. From September 2016 to September 2018, he studied as an exchange student at the National Institute for Materials Science (NIMS) in Japan. His recent research interests include the design and synthesis of advanced nanostructures for electrochemical energy storage and conversion.

Wei Ma is a professor of the School of Chemical Engineering at the Zhengzhou University. He received his bachelor degree in Inorganic Nonmetal Material Engineering from the Central South University in 2009 and obtained his PhD degree in Mineral Material Science from the Central South University in 2015. He studied in NIMS as a joint PhD student from September 2013 to September 2015. Since 2016, he has worked for the Zhengzhou University. His major work is focused on the fabrication of layered materials and electrochemistry.

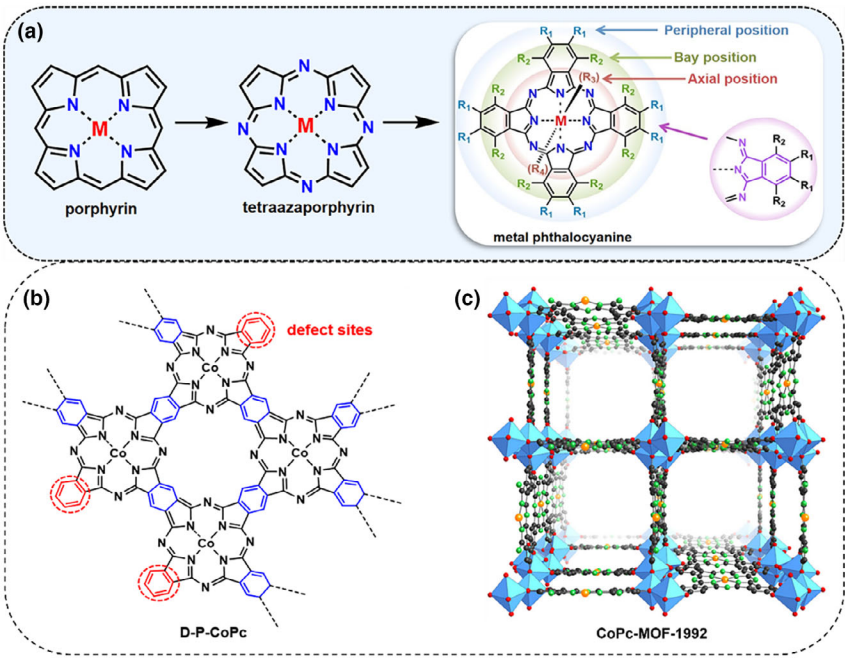

Figure 2. Molecular structures of MPcs and conjugated MPcs. a) The basic derivative process of phthalocyanine macrocycle and MPc molecular structure with descriptive terminologies for relevant positions around the molecule highlighted. Reproduced with permission from Ref. [31]. Copyright 2015, American Chemical Society. b) The structural diagram of the D-P-CoPc structure unit with highlighted signs and descriptive terminologies. c) The structural diagram of CoPc-MOF-1992. Reproduced with permission from Ref. [45]. Copyright 2019, American Chemical Society.

synthetic heterocyclic compounds MPcs whose four benzene rings expand the conjugated system endowed with good electroactivity themselves.[27,28] The structure of MPcs was tuned by introducing different types of substituents at the peripheral and/or bay positions and intercalating different central ions coordinated to the Pcs.[29–31] Toward the electrocatalysis application, Jasinski applied CoPc to the cathode of fuel cells without precedent in 1964. This pioneering work showed that CoPc exhibited remarkable electrochemical performance for the reduction of oxygen molecules in alkaline electrolytes.[24,32,33]

At present, MPcs (M = Fe, Co, Ni, and Cu) are the most widely used MPc-based catalysts. In some specific cases, MPcs can be oxidized and/or reduced to different valence states, such as Fe(II)↔Fe(III) and Co(II)↔Co(III). Among the metal ions with oxidation valence higher than +2, MPc molecules with smaller ionic radii tend to generate axial ligands, such as Al(III)Pc–Cl or Mn(III)Pc–Cl.[34] The presence of axial ligands tends to influence the M–N_4 catalytic activity through asymmetric geometrical configurations provided by mechanistic modeling.[35,36] While metal ions with much higher coordination numbers (i.e., rare earth metals) have larger ionic radii and may form sandwich-like metal complexes (symmetry/asymmetry).[37,38] Due to π–π interactions, MPcs are capable to show low-dimensional inferior conductivity along the column direction after crystallization.[39] With the charge increase of the central ions, more electric field strength and higher ion potential are obtained.[40,41] The variation of central ions leads to the difference in the framework and stacking patterns, which enables the optimization of the physicochemical properties of MPcs and their analogs.

Considering that MPc small molecules themselves possess poor electrical conductivity and chemical stability as those described earlier, it is reasonable to speculate that assembling the unit molecules into highly ordered crystal structures with enhanced physicochemical properties would be an ideal way to overcome these problems. Here, MPc-based conjugated frameworks based on molecule modular constructions can exhibit superior competitive advantages and features, such as unique surface interactions, charge transport, electromagnetism, and electrocatalytic function, which have great potential for further development. The ability of MPc frameworks, for instance, unique electrochemical performance, is due to their specific stacking orientation and excellent π–π overlap of the MPc units. Previous studies have demonstrated that conjugated MPc copolymers showed increased electrocatalytic performance over the monomers.[42–44] In this context, MPc-based frameworks can offer extended conjugated structures, high porosity, enlarged specific surface area, redox-active surface, and increased active sites accessibility. For example, the defective polymeric CoPc (denoted as D-P-CoPc in Figure 2b) exhibits considerable potential in the CO_2RR owing to the synergistic effect between the improved surface CO_2 binding affinity and electron-rich state in defective sites of the active frameworks, which may be ascribed to the concentration of higher π–electron conjugation environment in the active sites.[45] CoPc-MOF-1992 with a high-conductive framework exhibits accessible Co active sites with charge transfer properties to promote the reduction of CO_2 to CO (Figure 2c).[46] The polymers as electrocatalysts participate in concerted multielectron reduction. In addition, the enhanced charge delocalization in polymeric systems may increase not only the electron density at the core metal ions but also the electronic conductivity of the complex.[47] Therefore, reasonable module architectures and designs of MPc conductive framework materials based on functional building blocks present a perspective opportunity for scientific research of reticular chemistry.

The 18-π electron-conjugated structure of the inner 16-membered ring dominates the spectroscopic properties of MPcs. In general, the electronic absorption of MPc molecules consists of two strong bands, corresponding to $\pi(a_{2u})$-$\pi^*(e_g)$ (B band) and $\pi(a_{1u})$-$\pi^*(e_g)$ (Q band) transitions, which appears in the ultraviolet region around 300–400 nm and the visible region at 600–700 nm, respectively (**Figure 3**a,b).[48,49] The orbital energy level difference of electrons from the highest occupied molecular orbital (HOMO) to the lowest unoccupied molecular orbital (LUMO) is closely related to the Q band, while the B band is less affected by the external environment, and attributed to the material itself.[49,50] The positions of characteristic bands (especially the Q band) tend to shift (red shift/blue shift) with the type and connection of central metal ions, the substituent group of peripheral/bay position, solvents, and the strength of conjugation.[50,51] In addition, the charge transfer transition state (CTTS) is also shown due to the interaction of charge transfer between ligand and metal (Figure 3c).[52,53] Furthermore, the introduction of substituents and copolymerization may cause a significant change in the electron configuration on the MPcs ring, thus resulting in a shift of the Raman peak. The in situ electronic spectrum measurements thus provide an ideal platform for the characterizations

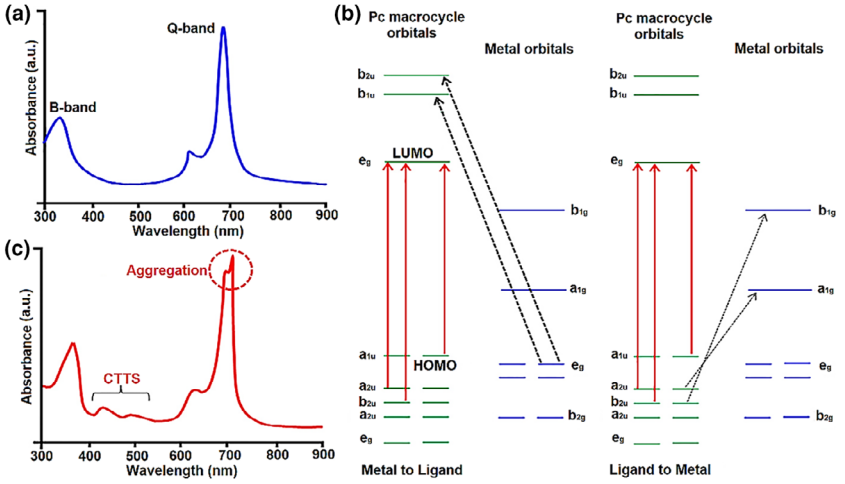

Figure 3. Typical electronic absorption spectra of MPcs. a) B and Q bands, b) Gouterman's four-orbital model, and c) CTTS. Reproduced with permission from Ref. [53]. Copyright 2022, Elsevier B.V.

of the real-time changes of MPcs, such as the evolution of atomic valence bonds and structure during the reaction, which have also become one of the supporting means to determine the rate-determining step (RDS).

3. Synthesis of Metallophthalocyanines

The research on MPcs has been going on for nearly a 100 years. Through the coordination of a simple ligand unit with the central metal ion, MPc is formed as a metal macrocyclic structure, where the metal ion acts as a template. Two synthetic ways are widely used for the preparation of MPcs: one uses phthalonitrile as the raw material, while the other adopts phthalic anhydride as the starting material (**Figure 4**).[16] Some precursors containing double-bond functionalities also be used, such as phthaloamides, phthalic acid, and isoindole-1,3-diimine. For metallophthalocyanine composites and conjugated metallophthalocyanines, the preparation approaches are summarized next.

3.1. Metallophthalocyanine Composites

Molecular modification over the carrier surface is suitable for applications requiring high electroconductivity. Over the past few years, diverse 2D phthalocyanine complexes, such as MPc/carbon, MPc/oxide, and MPc/MoS_2, have been successfully developed, offering a great

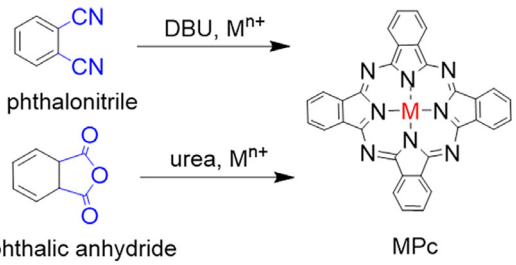

Figure 4. The common synthetic methods of MPcs.

possibility to expand the functionalities and applications.[54–57] For instance, based on π–π stacking interactions, the dispersion of reduced graphene oxide (rGO) and FePc in organic solvents (such as ethanol and dimethylformamide [DMF]) resulted in the target production at room temperature with the aid of ultrasound (**Figure 5a**).[58] Figure 5b shows FePc on rGO sheets, in which FePc was prone to agglomerate with an average size of 40–50 nm. However, ideal hybrids assembled by thinner nanosheets have not yet been achieved and are still expected. Kenichiro Irisa et al. reported the nanocomposite without aggregation, which was developed by electrochemically reducing a combination of monolayer GO dispersion and well-dispersed FePc in $CHCl_3$ (denoted the composite as ER(FePc/GO)).[59] In this procedure, the adsorbed atoms in solution reach the lattice growth point by surface diffusion, thus gradually inducing nucleation and subsequent crystallization, as evidenced by the signals of restacked GO and recrystallized FePc in Figure 5c. This preparation method for MPc-based nanomaterials is quite fast, scalable, and rarely limited by nanograin size or shape restrictions. In addition, the addition of the alkoxy chains on the periphery of the heterocycle helps to inhibit the aggregation of MPcs on the graphene sheets and further controls the morphology/structure of samples. For example, a sterically hindered CoPc could be immobilized on the surface of chemically converted graphene by π–π stacking.[60] Besides, plasma technology is a powerful tool for surface modification of materials due to its significant etching ability. CoO_x/CoPc was achieved on the CoPc surface by the growth of CoO_x nanodots under O_2 plasma treatment (Figure 5d).[61] The morphology of CoO_x/CoPc changed dramatically with the treatment duration. Specifically, a layered structure consisting of small particles and a large number of pores was formed on the surface of the CoO_x/CoPc-10 sample at a treatment time of 10 min (Figure 5e). The successful formation of highly crystalline nanodots in situ grown layered structure and interfacial structure with CoPc, as evidenced by Figure 5f,g, shows that the surface exposed Co atoms in CoPc are oxidized by oxygen plasma to form CoO_x, making the solid powder color from purple to black.

On the other hand, non-carbonous 2D substances such as MoS_2 have also been widely studied as supporters to anchor FePc molecules. FePc/MoS_2 hybrid nanostructure prepared by a one-step solvothermal process in which FePc and ammonium tetrathiomolybdate ($(NH_4)_2MoS_4$) were adopted as the starting materials (**Figure 6a–c**).[62] The annular dark-field (ADF) STEM and XRD pattern confirmed MoS_2 as 1T' phase in the product (Figure 6d,e), while the HRTEM image as depicted in Figure 6f revealed that the d_{002} interlayer spacing of MoS_2 layers increased to 9.5 Å, and the distance between the intercalated FePc and MoS_2 layers is ~3 Å, confirming the alternate assembly of FePc with 2D MoS_2 sheets. Furthermore, organics also hold great prospects as supporting substrates for the construction of MPc-based nanocomposites. As an example, FePc-loaded Ni–MOF nanosheets (named FePc@Ni–MOF) were prepared by an ultrasound-assisted solution technique (Figure 6g,h), in which 1,4-benzenedicarboxylicate (H_2BDC), $NiCl_2 \cdot 6H_2O$, and FePc were dissolved or dispersed in a mixed solvent of DMF, ethanol, and water to obtain a well-blended suspension.[63] After continuous sonication, uniformly deposited FePc on the 2D MOF

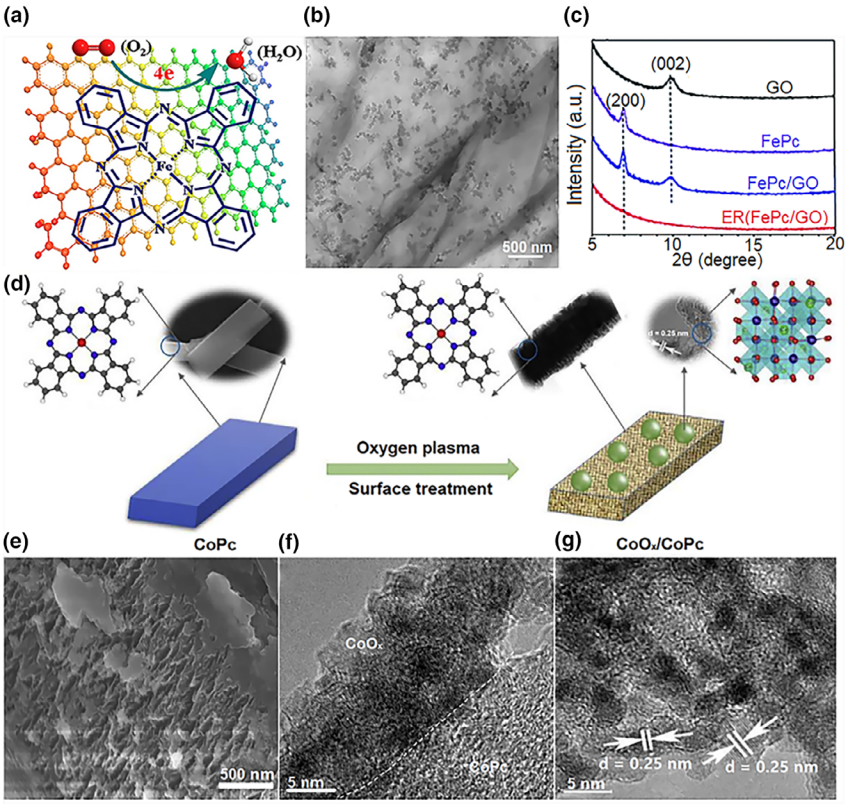

Figure 5. The synthesis of supported MPcs. a) Schematic illustration of the interaction between Graphene and FePc toward ORR process. b) TEM image of FePc/rGO composite. a, b) Reproduced with permission from Ref. [58]. Copyright 2013, American Chemical Society. c) XRD patterns of GO, FePc, GC-plate FePc/GO, and ER(FePc/GO). Reproduced with permission from Ref. [59]. Copyright 2021, RSC Adv. d) The illustration for the synthesis process of CoO_x/CoPc samples treated with O_2 plasma. e) SEM and f, g) HRTEM images of CoO_x/CoPc-10 sample. e–g) Reproduced with permission from Ref. [61]. Copyright 2022, Elsevier Ltd. A.

was obtained. Compared with inorganic substances, organic counterparts may provide infinite choices for the design of advanced electrocatalysts. The above cases have evidenced the vital roles of supporters in tuning the electrocatalytic activity. Further explorations may be focused on the design and development of novel conductive substrates for the improvement of practical applications, particularly in catalysis fields.

3.2. Conjugated Metallophthalocyanines

The construction of conjugated MPc copolymers is considered one of the effective strategies to alleviate sluggish electron transfer as well as molecule agglomeration. MPcs and their analogs can be polymerized to form a class of MPc-based 2D-conjugated frameworks with target structures and functions via rational design and modular construction of the molecular structure. In particular, under high-temperature conditions, MPcs can typically occur cyclotetramerization taken 1,2,4,5-tetracyanobenzene (TCB) or pyromellitic anhydride as precursors, which has been described for the preparation of the corresponding 2D network metallic polyphthalocyanines (MPPcs) (**Figure 7**). These as-obtained pure polymers have an exceptional electronic conductivity along the planar structures, which are comparable with semiconductors or even conductors.[64,65] Different connecting groups may provide more options for the diversity of polymers, which tunes the physicochemical properties.

Based on the rational design of COF materials, both the shape of the monomer component and the molecular configuration of the connection point not only determine the synthetic network topology, molecular scale, dimension, and electronic arrangement, but also directly affect the pore structure and morphology. For the functional design and property optimization of materials, structural units with large conjugated delocalized π electrons, such as olefin, pyrene, porphyrin, and triazine, are usually introduced.[66-68] After continuous exploration, a variety of organic reactions including several typical condensation reactions (such as Schiff base condensation, dehydration self-polycondensation or hydroxyl condensation of boric acid, and cyano self-polymerization) have been developed for building MPc grid materials.[69,70] The cross-coupling reaction is an attractive pathway to connect and assemble MPc organic monomers due to the efficient selectivity for a specific target molecule, in which two organic units are highly coupled to build a single molecule. Based on this, a piperazine-linked COFs was developed with high electrical conductivity and stability.[71] Furthermore, Yue et al. designed two novel bimetallic polyphthalocyanine COFs with high crystallinity, including $CuPcF_8$-CoPc-COF and $CuPcF_8$-CoNPc-COF, using MPc molecules nucleophilic aromatic substitution reaction.[72] Typically, the nucleophile interacts with the leaving group, which can occur on the benzene ring with special active groups such as strong electron-withdrawing substituents. While for MOFs, the organic ligands of the MPc units and bridged metal single atoms/clusters can function as immobilizing reactive sites during the catalytic conversion, leading to differences in the electron mobility of the entire framework, and thereby determining the catalytic performance of MOFs. The structure of MOFs is highly functional, and a variety of topological molecules can be formed by adjusting the number of dentitions of ligands.

Furthermore, ultrathin 2D nanosheets have been gifted with considerable potential because of the unexpected physicochemical properties that differ from their bulk counterparts. More active sites in favor of carrier mobility of nanosheets and can effectively improve electrical conductivity. Until now, conjugated MPcs nanosheet-layered materials, i.e., 2D MPcs COFs (MOFs), have been extensively reported following top-down and bottom-up methods.[73] The top-down methods mainly utilize peeling technology to destroy the noncovalent interaction between neighboring layers by an external force.[74] These allow the disintegration of the bulk structure to produce unilaminar or few-layer nanosheets with large lateral dimensions. Through manual/mechanical ball milling or liquid-phase exfoliation methods, the interlayer interactions of the bulk crystals are disrupted and the ultrathin nanosheet-like structures are thus achieved. Wang et al. first synthesized regular bulk

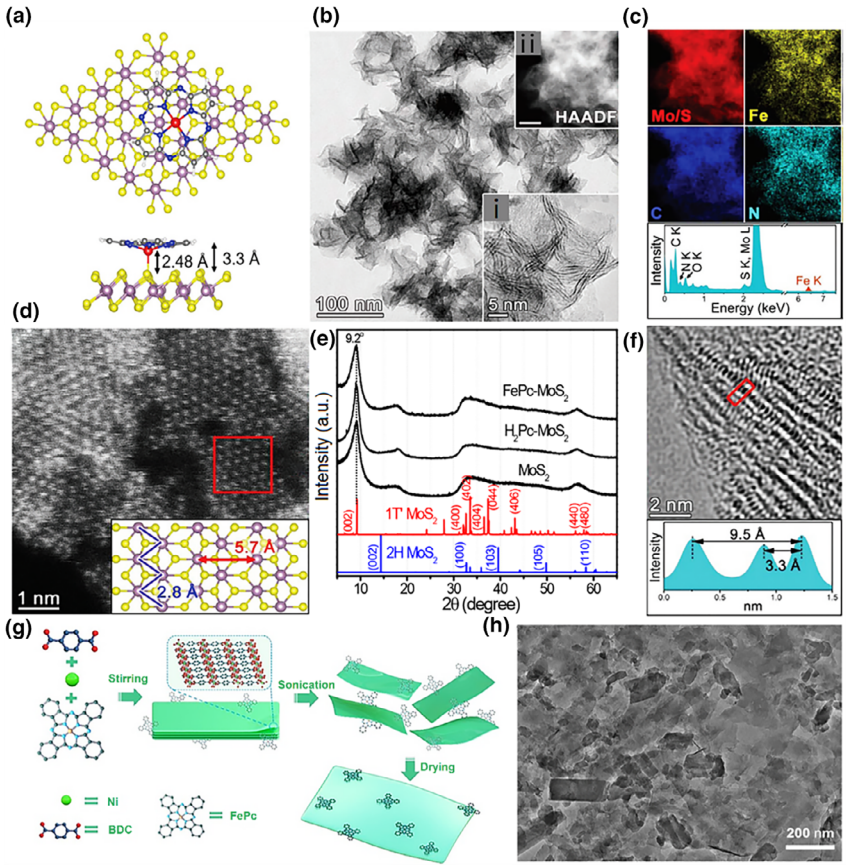

Figure 6. The construction and characteristics of MPc composites. a) Optimized structures (the ball-and-stick model) of the 1T′ phase MoS_2-FePc in the top and side views. b) i) HRTEM image showing the general morphology of the FePc-MoS_2 hybrid complex and ii) high-angle annular dark-field scanning TEM (HAADF-STEM) image. c) EDX elemental mapping of FePc-MoS_2 hybrid. d) Atomically resolved ADF STEM image of the basal plane and the simulated atomic structure. e) XRD patterns of FePc-MoS_2, H_2Pc-MoS_2, and MoS_2 complexes. f) Lattice-resolved TEM images for the side plane and their intensity profile across the interlayers. a–f) Reproduced with permission from Ref. [62]. Copyright 2019, The Royal Society of Chemistry. g) Illustration of the synthesis process and h) TEM image of FePc@Ni-MOF nanocomposite. g, h) Reproduced with permission from Ref. [63]. Copyright 2021, American Chemical Society.

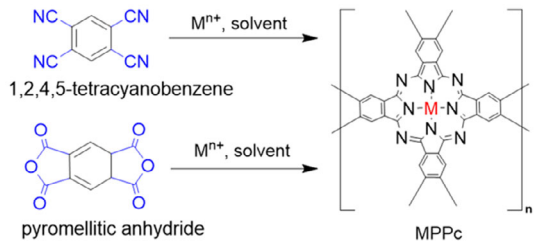

Figure 7. The common synthetic methods of reticular MPPcs.

Ni_2[CuPc(NH)$_8$] crystals, and then thin Ni_2[CuPc(NH)$_8$] nanosheets were obtained with a yield of 40%–50% by exfoliating the bulk precursor through a ball milling mechanical method (**Figure 8a**).[75] During the exfoliation process, NaCl/KCl as an intercalating agent was crucial in lowering the shear forces of adjacent interlayers and enabled the mild delamination of the stacked MOF layers. As evidenced by the atomic force microscopy (AFM) image, the thickness of the resulting nanosheets was ~7 nm, corresponding to approximately 10 monolayers (Figure 8b). In addition, through adding different edge sealing agents in polymer precursors, selective edge functionalized 2D thin layers conjugated aromatic networks CAN-Pc (Co)-x (x = o, n, b, and p, which represent four different edge structures, namely phenyl, naphthyl, tertbutyl phenyl, tetraphenyl) were exfoliated by ball milling (Figure 8c,d).[76] The marginal modification of acid anhydride substituents can increase the interlayer distance at the edge while decreasing the π–π interaction. During the ball milling, the small balls in the grinding cylinder collide and squeeze each other to strip off the bulk CoPPc-x into nanoplates. While in ultrasonic liquid phase delamination processes, an appropriate control agent can bring great benefits to the delamination process. Bulk ethynyl-linked MPc-conjugated polymers (CPs) were prepared from two phthalocyanine monomers M[Pc(I)$_4$] and M[Pc(ethynyl)$_4$] via a coupling reaction.[77,78] Through the subsequent solvent-assisted liquid sonication, the bulk MPc-CP materials may be exfoliated into ultrathin 2D nanosheets (**Figure 9a**). Taking the bimetallic compound $Fe_{0.5}Co_{0.5}$Pc-CPs as an example, the yield ratio of $Fe_{0.5}Co_{0.5}$Pc-CP nanosheets (NSs) can reach up to ~36% and 51% for 2 and 8 h, separately, after the homogeneous dispersion of the copolymer in ethanol followed by ultrasonic stripping. $Fe_{0.5}Co_{0.5}$Pc-CP NSs showed a smooth surface with a uniform thickness of ~1.05 nm, corresponding to three monolayers (Figure 9b,c). It should be noted that after the delamination process, the crystalline precursor was transformed into the amorphous phase structure (Figure 9d–f). The bright dotted regions observed in the aberration-corrected HAADF-STEM image are attributed to single Fe/Co–N_4 coordination sites in the $Fe_{0.5}Co_{0.5}$Pc–CP NSs framework. However, the low yield of as-exfoliated few-layer films restricted by the aggregation effect needs to be further improved.

Additionally, the bottom-up approach is another conventional strategy for the direct preparation of ultrathin sheet-like nanostructures through controlled crystal growth along lateral orientation.[78,79] As the combined merits of simple operation and facile control, hydrothermal/solvothermal procedures are the most popular bottom-up methods for MPcs. In such closed systems, reactants are usually mixed and/or dispersed in an aqueous /nonaqueous system to achieve the purpose of the reaction with all of the dissolution, dispersion, and chemical reactivity of the reactants greatly improved. Yi et al. successfully synthesized conjugated 2D NiPc–NiO_4 MOF nanosheets of AA stacking with a thickness of 1.65 nm (i.e., ~5 layers) by the reaction of nickel phthalocyanine-2,3,9,10,16,17,23,24-octaol (NiPc–OH) and $Ni(OAc)_2{\cdot}4H_2O$ in water at 85 °C for 24 h (Figure 9g–k).[80] Besides, surface-mediated synthesis guides the preparation of conjugated MPcs nanolayers under ultrahigh vacuum or liquid conditions. For example,

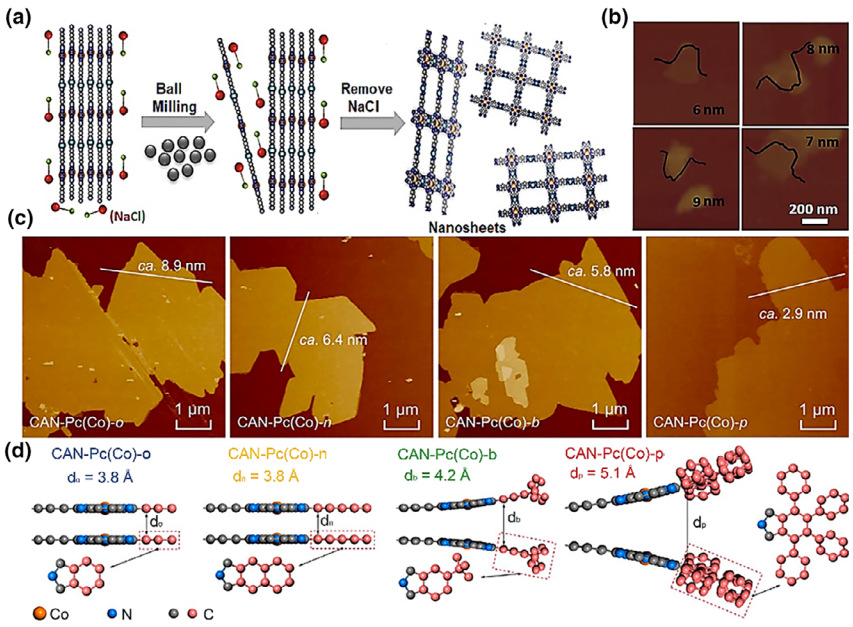

Figure 8. The preparation of conjugated metallophthalocyanines. a) Schematic illustration of the exfoliation of bulk $Ni_2[CuPc(NH)_8]$ 2D c-MOF into nanosheets. b) AFM images of $Ni_2[CuPc(NH)_8]$ 2D c-MOF nanosheets. a, b) Reproduced with permission from Ref. [75]. Copyright 2020, Wiley-VCH Verlag GmbH & Co. KGaA, Weinheim. c) AFM images of CAN-Pc(Co)-x. d) A schematic representation of the edge expansion of CAN-Pc(Co)-x caused by the presence of the edge-functionalized anhydride groups. c, d) Reproduced with permission from Ref. [76]. Copyright 2020, American Chemical Society.

K. Selvaraju et al. fabricated Co-based polyphthalocyanine nanosheets via 2D packaging arising from a metal-oriented surface reaction, in which the reactant TCB was mixed with anhydrous cobalt chloride ($CoCl_2$, a precursor and catalyst for CoPPc-based materials) and quinoline.[81] Through mild directed surface reaction engineering, porous nanosheets with highly ordered atomic structures were formed in microwave treatment (e.g., 800 W for 10 min). The detailed comparison of the synthetic methods for 2D layered MPc nanosheets is summarized in **Table 1**. Considering the excellent electron transport capability over 2D planes, ultrathin polymeric MPc nanosheets are admirable candidates. Moreover, it is believed that when such MPc copolymers are assembled with redox-active inorganic materials (2D counterparts in particular), the electrocatalytic performance will reach new heights because of the strong interfacial coupling effect.[82,83] Therefore, the rational screening and accurate structure design of the catalyst laid a solid foundation for the development of the electrocatalysis field.

4. Electrocatalytic Energy Conversion of MPc-Based Catalysts

4.1. ORR

4.1.1. Electrocatalytic ORR Mechanism of MPcs

Oxygen widely existing in nature has relatively high redox potential and is utilized as a readily available gas for energy conversion in sustainable energy conversion systems, like the core cathode of fuel cells.[83–86] The ORR is a complex electron transfer process, which occurs via either a direct or indirect four-electron ($4e^-$) transport pathway.[87] Considering the energy conversion efficiency, the direct $4e^-$ reduction pathway, i.e., the reduction of oxygen into water or hydroxyl ions (in acid and alkaline electrolytes, respectively), is generally expected.[88,89] The reaction mechanisms of the ORR are expressed in **Figure 10a**.[90]

The direct transfer mechanism of ORR can be zoned into dissociative and associative processes in essence. For the catalytic process of the MN_4-based species, there are two possible modes of adsorbed oxygen: side-on (shoulder-type) adsorption and end-on adsorption configuration.[91,92] Previous studies have demonstrated that the end-on oxygen configuration tends to be more stable for an O_2 molecule adsorbed on M–N_4 sites.[93] In the real system, heterolateral coadsorption may also occur. For MPc materials, the well-defined active site structure makes it an excellent candidate for efficient ORR. Importantly, the ORR activity is associated with electrochemical and electronic properties such as metal redox potential, binding energy of oxygen-containing intermediates, d-orbital electrons, and energy levels.[94] The M(III)/M(II) redox potentials as mediators should be close to ORR potential to drive the occurrence of the ORR. Therefore, the ORR activity of MPcs can be optimized by structural modifications on the Pcs framework to regulate the M(III)/M(II) redox potentials. In many studies, it has been reported that electron-withdrawing/donating groups have a shift of Fe(III)/Fe(II) redox potential, showing the enhancement of ORR activity. As shown in Figure 10b, a linear scaling relationship (LSR) related to M(III)/M(II) redox potential for various MPc catalysts has been defined.[94] In addition, for ORR, the binding energy of three intermediates (M–O, M–OH, and M–OOH) is highly correlated, which governs the overall ORR kinetic process.[6,95] The Gibbs binding energy of M–OH (denoted as ΔG_{OH}) at metal active sites is often devoted to predicting ORR performance. At the same time, the enhanced M–OOH stability contributes to a greater limiting voltage and activity enhancement.

Particularly, chelated MPcs-conjugated copolymers are regarded as promising Pt substitutes, having latent capacities toward ORR in terms of catalytic activity, conductivity, and reaction rate.[96,97] It has been confirmed that the MN_4-conjugated structure of phthalocyanine species is the main catalysis active sites.[98] The d-band center of metal sites plays a role in the reaction kinetics in MPc-based materials. For instance, when MPc monomers are polymerized, the longer conjugated structure of MPPcs leads to electron localization and richer electrons at the metal sites, which is beneficial for regulating the adsorption of intermediates for boosting ORR. However, the precise interpretation of the ORR mechanism with MPPcs, especially the RDS acting on the metal centers and the possible contribution of coexisted C–N, is still controversial. The dynamic structural changes of active units during ORR also remain elusive. Especially, for MPcs/MPPcs with axial coordination, it is necessary to rationally speculate on the effect of the regulatory mechanism of the axial ligand on the electronic structure of transition metals.

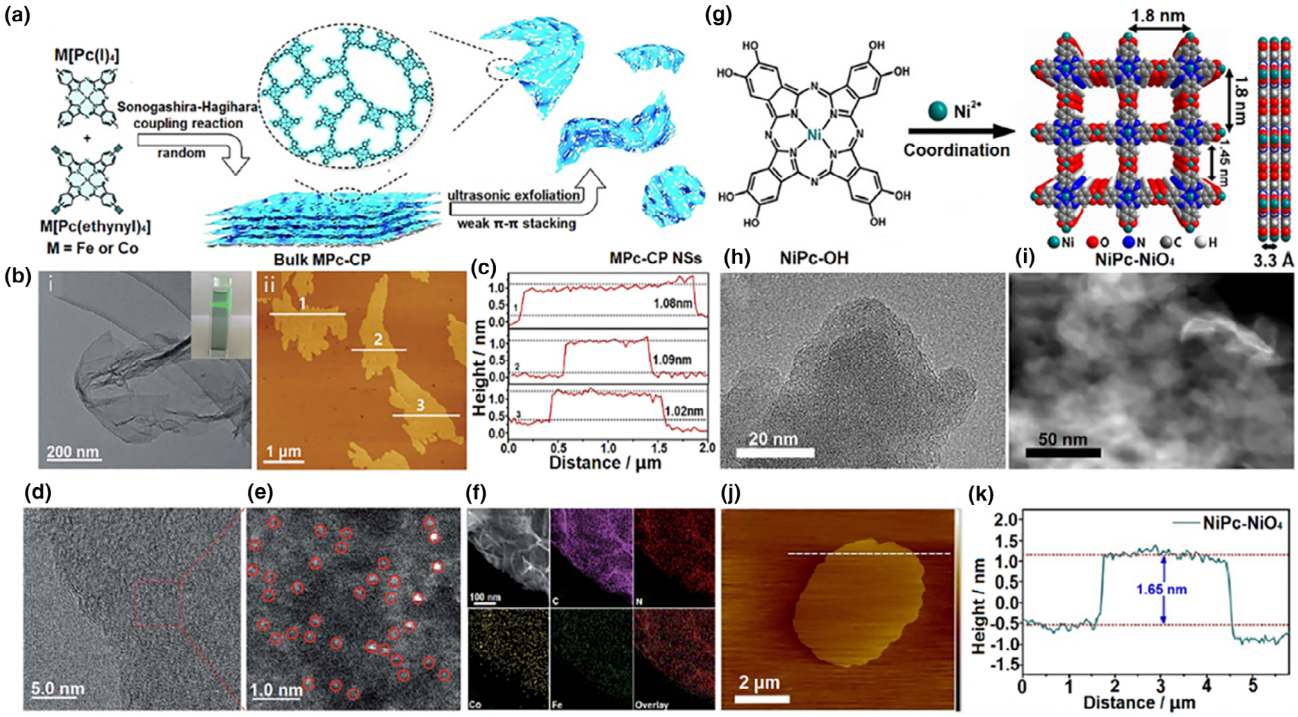

Figure 9. Preparation and characterization of MPcs nanosheets. a) Schematic illustration of synthetic $Fe_{0.5}Co_{0.5}$Pc-CP NSs. b) i) TEM and ii) AFM images of $Fe_{0.5}Co_{0.5}$Pc-CP NSs. *Inset*: Photograph of the Tyndall effect of the $Fe_{0.5}Co_{0.5}$Pc-CP NSs suspension. c) The corresponding height profiles of $Fe_{0.5}Co_{0.5}$Pc-CP NSs. d) AC STEM image and e) enlarged image of the $Fe_{0.5}Co_{0.5}$Pc-CP NSs (single Fe/Co atoms are highlighted by red circles). f) HAADF-STEM image and elemental mapping of C, N, Co, and Fe of the $Fe_{0.5}Co_{0.5}$Pc-CP NSs. a–f) Reproduced with permission from Ref. [77]. Copyright 2019, The Royal Society of Chemistry. g) Illustration of the preparation of NiPc-NiO_4 nanosheets (top and side view of their structures with 2 × 2 square grids in AA-stacking mode). h) TEM and i) HAADF-STEM images of NiPc-NiO_4. j) AFM image of NiPc-NiO_4. k) The height profile along the white line of NiPc-NiO_4. g–k) Reproduced with permission from Ref. [80]. Copyright 2021, Wiley-VCH GmbH.

4.1.2. MPc-Based ORR Catalysts

Limited by intrinsic properties and natural origin, MPcs itself suffer from inferior electrical conductivity and modest catalytic efficiency toward ORR, therefore further elaborate modifications were required.[25,99] Surface loading on conductive support to effectively promote the potential generation of ORR has been widely reported. First, MPcs can be immobilized through noncovalent π–π interactions. MPc planar macrocyclic structures can be easily adsorbed on the surface of conducting substrates (e.g., graphene and carbon nanotubes [CNTs]) to form stable hybrid nanomaterials as electrocatalysts to enhance ORR activity via strong π–π interactions. Second, the introduction of exo-ligands makes MPc attached to support vectors, though this often requires preliminary modification of the supports. For instance, the surface of graphene can be structurally functionalized by grafting different functional groups to improve reactivity and conductivity.[100] Fe-PyNGs were fabricated by anchoring tightly FePc on pyridine cycloaddition of graphene sheets (PyNGs).[101] As a result of the synergistic effect, the as-prepared Fe-PyNGs showed higher electrocatalytic activity than both FePc and FePc/NGs samples in alkaline media. Besides, modifying the surface of conductive carbon materials (acetylene black) with oxygen-containing groups (such as AB-O) has been evidenced to effectively induce electron localization of axially positioned O–FeN_4, affecting the electron symmetry distribution of Fe centers, and thus promoting the O_2 adsorption and activation ability (**Figure 11a**).[102] The optimized FeAB–O catalyst shows a Tafel slope of 27.5 mV dec^{-1} and a half-wave potential ($E_{1/2}$) of 0.90 V (vs reversible hydrogen electrode [RHE]), which is superior to that obtained by physical mixing without axial oxygen coordination (FePc/AB) and Pt/C benchmark (Figure 11b,c). While for the noncarbonaceous supports (e.g., MoS_2), the FePc–MoS_2 hybrid complex shows comparable conductive properties with 1T' MoS_2, and thus an activity enhancement toward ORR is created (Figure 11d,e).[62]

In addition, 2D-conjugated polymers (MOFs and COFs) resulting from the MPc encapsulation technique were demonstrated to be a designable porous organic material with enhanced ORR activity because of the high controllability and abundant exposed active sites.[103,104] It is desired to develop ORR electrocatalysts with well-defined and tunable M–N_x central structures of excellent intrinsic conductivity and durability. On the one hand, large conjugated reticulated blocks with functionalized modulation at the molecular level have been engineered to show promising ORR behaviors. The bridging structure of the bulk monomers affects the catalytic performance. In 2019, Zhong et al. designed a hyperconjugated polymer PcCu-O_8-Co MOF catalyst linked by Co–O_4 bridges for efficient ORR because of the homogeneous distribution of well-defined dual sites and efficient mass transfer pore channels (Figure 11f–h).[105] It is theoretically revealed that the enhanced ORR catalytic performance can be attributed to the bridged Co–O_4 building block with high ORR activity. The strong interaction between the σ* antibonding orbital ($e_g = 1$) of the Co node and the unpaired

Table 1. Synthetic methods for 2D MPc nanosheets.

Strategies	Approach	Advantages	Disadvantage	References
Top-down	Mechanical exfoliation (manual or ball milling)	• A simple and easy application to exfoliate layered MPPc with interlayer π–π conjugation. • It can be used for dry or wet grinding with a wide range of operating conditions. • The method can be operated continuously or intermittently. • Large-scale preparation of 2D monolayer/few-layer nanosheets can be achieved.	• Ball mills are bulky and heavy, and operate with strong vibration and noise. • Lower work efficiency and yields. • High machinery costs and energy consumption. • Intercalating agents often need to be introduced into the system to decrease interlayer interaction.	[75,76]
	Ultrasonic-assisted exfoliation	• A gentle, simple, and low-cost exfoliation method. • It is less demanding in terms of preparation conditions and low-cost and simple.	• The number and size of exfoliated layers of as-obtained nanosheets are not easy to control. • The nanosheets are prone to aggregation, and therefore have a lower yield.	[77,78]
	Chemical exfoliation	• Time-saving and efficient.	• Relatively complex to operate, even inert gas protection is required during preparation.	[78,79]
Bottom-up	Solvothermal synthesis	• Scalable and easy to control. • Clean and efficient. Additional solvents are not used in the reaction process.	• High-energy consumption, and high-temperature and pressure conditions are often required.	[80]
	Surface/interface synthesis	• A directed on-surface/interfacial reaction engineering. • Easy to operate, mild conditions, and friendly environment. • The morphology and thickness of as-prepared nanosheets can be controlled.	• Synthesis is difficult, and often does not meet the dimensional requirements of the materials we need.	[81]

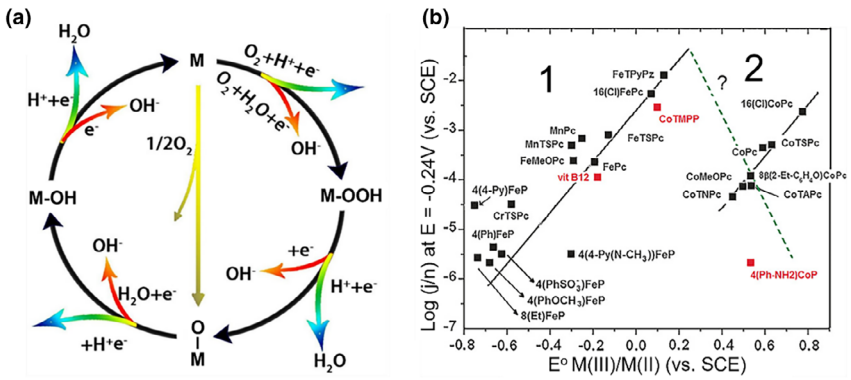

Figure 10. Electrocatalytic ORR mechanism for MPc-based materials. a) ORR electrolysis mechanism with MPc units in acidic (blue line) and alkaline (red line) electrolytes (where M represents catalytic active site). Reproduced with permission from Ref. [90]. Copyright 2020, Elsevier Ltd. b) Plots of catalytic activities for ORR in alkaline media as current densities (j) divided by the number of electrons (*n*) involved in the reaction for different catalysts and recorded at $E = -0.24$ V versus SCE. $n = 4$ for Cr, Mn, and Fe catalysts, and $n = 2$ for Co catalysts. Reproduced with permission from Ref. [94]. Copyright 2016, Wiley-VCH Verlag GmbH & Co. KGaA, Weinheim.

electrons of the O 2p orbital improves the O_2 adsorption capacity. And the activation energy of breaking the O=O bond is reduced, which is beneficial to the reduction process of O_2 into H_2O. Combined with the advantage of the enhanced conductive surface matrix, PcCu–O_8–Co stabilized by CNTs achieved a high $E_{1/2}$ of 0.83 V (Figure 11i). In addition, the introduction of axial ligands enables the modulation of the MPc structures, which will concurrently bring dramatic changes in physicochemical nature such as electrical conductivity. Zhao et al. systematically expounded the effect of the axial ligands on the ORR catalytic activity of Fe–N_4 sites for FePPc in acidic and basic solutions.[106] The results indicated that FePPc-I showed the optimal catalytic performance in both electrolytes, especially in alkaline environments (Figure 11j). Meanwhile, a new descriptor intermolecular hardness (η_{DA}, indicating the energy gap between the dz^2 of the Fe center and p_x/p_y of *OH) was given to evaluate the ORR activity (Figure 11k). According to the crystal field theory, 3d orbital configuration and electron spin state of the Fe central atoms can be controlled by coordinating the atomic center with different ligands, thus optimizing the ORR performances (Figure 11l).

On the other hand, ultrathin nanofilms with ample specific surface area and cavity occupancy can supply sufficient catalytic sites for the adsorption/dissociation of target molecules, which may also influence ORR activity. Selvaraju et al. demonstrated well-organized Co-based polyphthalocyanine nanosheets (Co-PyPc NSs) electrocatalysts for ORR through 2D capsulation (**Figure 12**a).[81] The 2D MOF structure encapsulated by CoPc macrocycles can easily adsorb O_2 molecules to the Co–N_4 active centers. Meanwhile, the precise arrangement of molecules and the well-aligned pore structure provide electron transport pathways and enable a more direct reaction. The assembly of nanosheets substantially suppressed the aggregation of MPcs molecules and accelerated electron dispersion. Compared with the conventional 20% Pt/C electrocatalyst, the Co-PyPc NSs displayed an ascendant onset potential ($E_{onset} = 0.974$ V) and a diffusion-limiting current density

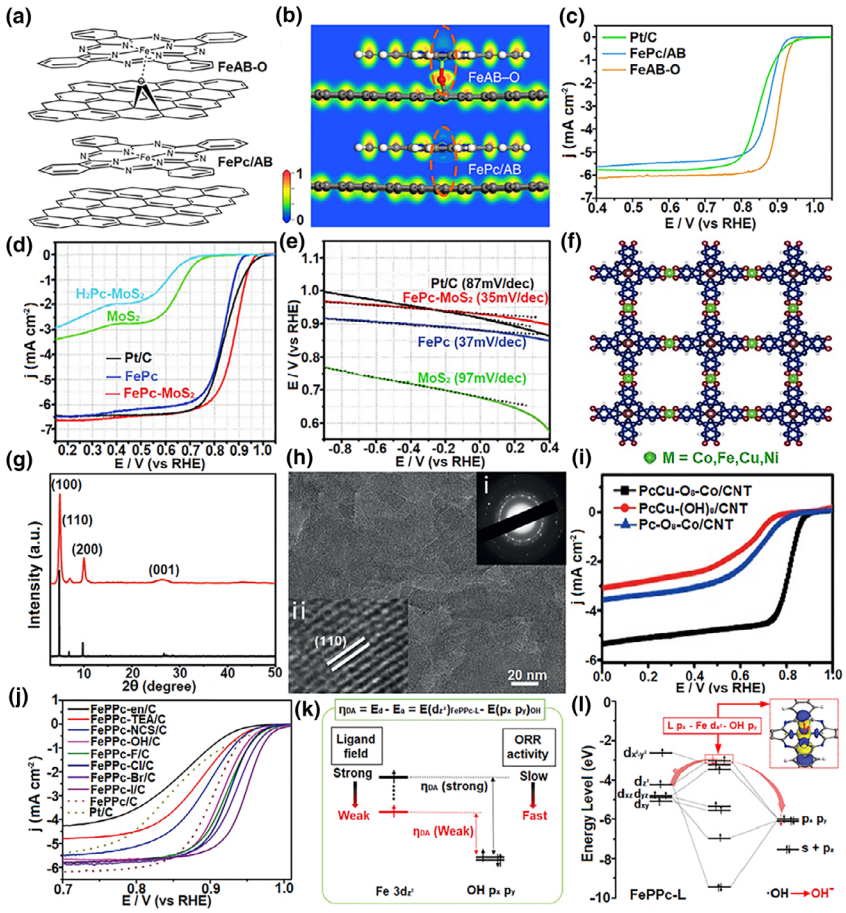

Figure 11. MPcs and its composites electrocatalysts for ORR. a) Molecular structure model illustrations of FeAB–O and FePc/AB. b) Electron localization functions of FeAB–O and FePc/AB. c) LSV curves of FeAB–O, FePc/AB, and Pt/C in O_2-saturated 0.1 M KOH for ORR. a–c) Reproduced with permission from Ref. [102]. Copyright 2020, Nature Communications. d) LSV curves of FePc-MoS_2, FePc, and Pt/C, H_2Pc-MoS_2, and MoS_2, for the ORR in O_2-saturated 0.1 M KOH. e) Tafel plots derived from the LSV curves. d, e) Reproduced with permission from Ref. [62]. Copyright 2019, The Royal Society of Chemistry. f) Schematic structure of as-prepared PcCu-O_8-Co. g) Experimental (red line) and simulated (black line) XRD patterns of PcCu-O_8-Co. h) TEM images of PcCu-O_8-Co. *Inset*: i) Selected area electron diffraction (SAED) and ii) HRTEM images). i) LSV curves of PcCu-$(OH)_8$-CNT, Pc-O_8-Co/CNT, and PcCu-O_8-Co/CNT for ORR. f–i) Reproduced with permission from Ref. [103]. Copyright 2019, Wiley-VCH Verlag GmbH & Co. KGaA, Weinheim. j) LSV curves at a scan rate of 10 mV s^{-1} of ORR on the as-prepared PFePc-L/C and Pt/C electrodes under a rotation rate of 1600 rpm in a 0.1 M KOH electrolyte. k) A new descriptor of η_{DA} between PFePc-L and *OH. l) Molecular orbitals of HO-PFePc-L. j–l) Reproduced with permission from Ref. [104]. Copyright 2022, Wiley-VCH GmbH.

($j_d = 4.61$ mA cm^{-2}) (Figure 12b). The weakened interlayer π–π overlap is capable of facilitating the exfoliation of the bulk $Fe_{0.5}Co_{0.5}$Pc-CPs into nanosheets via an ultrasonic exfoliation-assisted technique.[77] Attached to the graphene surface (Figure 12c), the resulting heterostructure $Fe_{0.5}Co_{0.5}$Pc-CP NS@G as an ORR electrocatalyst showed a more positive E_{onset} of 1.006 V, and the $E_{1/2}$ of 0.927 V in 0.1 M KOH medium (Figure 12d,e). This catalyst was further used as a cathode in Zn–air batteries to evaluate the full-cell applicability (Figure 12f), and the results showed more promising performance for $Fe_{0.5}Co_{0.5}$Pc-CP NS@G rechargeable battery (Figure 12g). Functionally customized structures of porous adsorption polymeric materials have been achieved by changing different cross-linking agents, promising enhanced electrical conductivity.[76,107] Based on this, Yang et al. prepared thin 2D-conjugated multimeric CAN nanosheets promoting the accessibility of O_2 to the surface electrocatalytic active sites toward ORR (Figure 12h).[76] This also leads to higher utilization of the Co–N_4 active unit, and thus an improved ORR current density (Figure 12i), indicating considerable improvement in activity for oxygen reduction through structural regulation and morphology design.

4.2. OER

4.2.1. Electrocatalytic Mechanism of MPcs for OER

OER releases oxygen through the water oxidation process, which can be considered as the reverse process of ORR. Because of the slow kinetics of the OER process, higher overpotential is often needed. The development of highly active catalysts is driven to address the complexity of the OER process occurring on the anode surface. Regarding MPc macrocyclic compounds, two possible pathways, involving three intermediates (M–OH, M–O, and M–OOH), occur in promising adsorbent evolution mechanisms to show excellent OER ability.[49,90,108] The metal active site part of MPcs often requires the absorption of H_2O molecules to form hydroxyl species. To predict the electrocatalyst activity of OER with MPc units, an intrinsic LSR between the interdependent adsorption energy of intermediates has been established, such as a volcano-shaped curve between ΔG_{*O}-ΔG_{*OH} and experimental overpotential at 1 mA cm^{-2} on various metal oxide surfaces.[109,110] Therefore, the efforts to break the limitations of LSR are in the spotlight.

Natalia Chebotareva et al. systematically elucidated the hydrolysis process which was catalyzed by the transition metal phthalocyanines.[53] It was confirmed that among the first-row transition metal elements, FePc, CoPc, and NiPc showed higher catalytic activity compared to ZnPc, MnPc, and CuPc, where NiPc had the lowest overpotential. Also, at lower potentials, the MPc-modified carbon electrodes have high OER efficiency. These great differences in MPc activity can be attributed to the correlation between the d-electron and first reduction potentials. This work also offers the possibility of further development of highly active MPc electrocatalysts toward OER.

For the MPc-based catalysts, their stability during OER is closely related to the formation of metal oxide or hydroxide at active sites, which has been widely concerned. It has shown that the decrease in stability of MPcs was affected by redox potentials. Generally, the OER process is mediated by the redox pairs of metals, but the activity and stability may decrease as the number of cycles increases. For example,

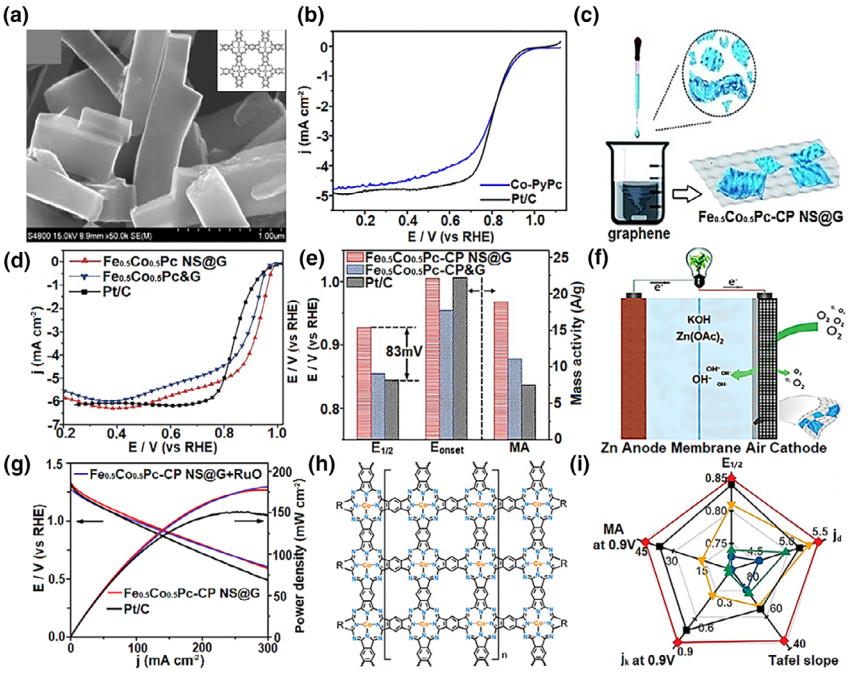

Figure 12. Layered metal phthalocyanine nanosheets toward ORR. a) SEM image of the Co-PyPc NSs electrocatalyst (*inset*: the structure of Co-PyPc NSs). b) LSV curves of Co-PyPc NSs and Pt/C at 1600 rpm. a, b) Reproduced with permission from Ref. [81]. Copyright 2019, Springer-Verlag GmbH Germany. c) Schematic illustration of synthetic $Fe_{0.5}Co_{0.5}$Pc-CP NS@G. d) LSV curves of $Fe_{0.5}Co_{0.5}$Pc-CP NS@G, $Fe_{0.5}Co_{0.5}$Pc-CP&G, and 20% Pt/C measured in O_2-saturated 0.1 M KOH solution. e) $E_{1/2}$, Eonset, and mass activity (MA) comparisons of $Fe_{0.5}Co_{0.5}$Pc-CP NS@G, $Fe_{0.5}Co_{0.5}$Pc-CP&G, and Pt/C (20%) in alkaline solution. f) Schematic diagram of the Zn–air battery. g) The discharge polarization plots and power density curves of the Zn–air battery. h–l) Reproduced with permission from Ref. [77]. Copyright 2019, The Royal Society of Chemistry. h) Schematic diagram of the molecular structure for CAN-Pc(Co)-x. i) Comparison of $E_{1/2}$, j_d, Tafel slope, kinetic current density (j_k), and MA for 20% Pt/C and CAN-Pc(Co)-x electrodes. h, i) Reproduced with permission from Ref. [76]. Copyright 2020, American Chemical Society.

the change in valence state from Fe(II)/Fe(III) into Fe(IV) will reduce the size of Fe ions in the MPc framework due to the shielding effect of Fe valence electrons, and thereby will affect the M–N bond and consequently result in the dissolution of metal ions from the Pc framework.[94] Therefore, it is expected that further improvement in OER performance by the adjustable electronic structure and redox properties of MPcs.

4.2.2. *Electrocatalysts Based on MPcs for OER*

The overall water splitting was slow kinetically hindered by the complex $4e^-$ transfer process of OER. Precious metal-based materials, such as Ir, Ru, and their metal oxides, have been widely accepted as state-of-the-art electrocatalysts due to their impressive OER catalytic activity, however, suffer from high cost, scarcity, and poor long-term stability.[109–111] In this aspect, the development of robust, stable, and low-cost catalysts suitable for large-scale market development is urgent.[112,113] Up to now, many modulation strategies have been demonstrated for MPc materials for enhanced OER activity. At the substrate composite level, through studying MPcs loaded on various carbonaceous substrates (such as G, nitrogen-doped graphene [NG], and defective graphene [DG]), it was found that structure tunability of the graphene enables DG with the excellent catalytic effect.[114] The axial interaction of the metal center Fe with the C atoms around the graphene vacancies may lead to the moderate adsorption of oxygen-containing intermediates to enhance the OER activity (**Figure 13**a–c). When nickel foam (Ni-foam) was used as a substrate, polymer CoPc-coated Ni foam showed enhanced conductivity with a low overpotential in the OER test range. The resulting combination of the synthesized samples with benchmark IrO_2 catalyst exhibited improved OER activity.[115] To improve the interface mechanism between matrix carbon and macrocyclic carbon to modulate OER behavior, the association with CNTs can not only achieve efficient immobilization of MPcs but also promote OER enhancement. Dai and his workers demonstrated that sulfonated CoPc/CNT hybrids (CoPc-SO_3H/CNT) showed much lower OER overpotential than the corresponding unmodified samples (Figure 13d,e).[116] This can be attributed to both the strong conductivity of CNT and the electron-modulating effect of peripheral electron-absorbing substituents promoting the OER shift toward a more favorable potential. FePc modified by pyridine axial coordination on CNTs (FePc-py-CNT) enhanced OER activity also was reported, which is ascribed to facilitating the adsorption of O_2 at the Fe-based sites due to the increase of Fe–N bond binding length in the fifth coordination site.[36]

With the continuous development of transition metal composites, it has been gradually discovered that functionalized Ni/Fe-based MOFs (COFs) possess further improved OER activity, relative to those of benchmark precious metal oxide catalysts. Nevertheless, due to the complex surface electronic structure of Ni/Fe-based OER electrocatalytic materials, the precise mechanism of action of the catalytically active sites remains controversial. In the early years, a 2D π-conjugated nickel phthalocyanine metal–organic framework (NiPc–MOF) with fourfold symmetry by bottom-up fabrication was developed for efficient water oxidation catalysis for the first time (**Figure 14**a).[117] The pH-dependent results revealed that the OER activity increases with the pH values (Figure 14b). This NiPc–MOF can also easily grow on various substrates, resulting in a significantly improved catalytic activity. In 2020, Qi et al. successfully developed a 2D strongly conjugated double heterometallic compound $Fe_{0.5}Ni_{0.5}$Pc-CP (Figure 14c).[118] The as-prepared $Fe_{0.5}Ni_{0.5}$Pc-CP exhibited prominent performance for OER in 1.0 M KOH solution, which is comparable to commercial RuO_2 (Figure 14d,e). The electronic synergy between adjacent Fe and Ni atoms in $Fe_{0.5}Ni_{0.5}$Pc-CP facilitated its oxidation to high-valent Fe/Ni species during electrocatalysis, thereby accelerating the OER kinetic rate. Until 2023, the OER performance of FeNi-based phthalocyanine MOF is further improved. The overpotential of conjugated bimetallic Fe/Ni-PPc for OER is 42/194 mV in 0.5 M H_2SO_4 and 1 M KOH, respectively, at a current density of 10 mA cm^{-2}.[119] To investigate the effect of electronic structure interaction with dual active sites on the electrocatalytic OER performance, Li et al. combined 2,3,9,10,16,17,23,24-octahydroxy MPcs via metal–oxygen ($M–O_4$) bonds to construct

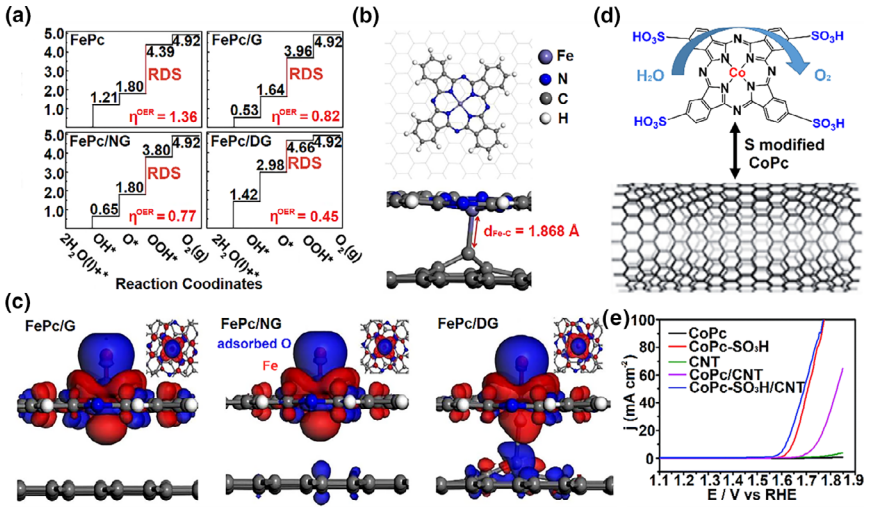

Figure 13. MPc and its composites for OER. a) The free energy diagrams of OER at $U = 0$ for pure FePc, FePc supported on pure G, NG, and DG. b) The geometric structure of DG. c) The charge density difference plots of O atom for FePc supported on pure G, NG, and DG. a–c) Reproduced with permission from Ref. [114]. Copyright 2021, Elsevier B.V. d) The geometric structure of CoPc-SO_3H/CNT. e) LSV curves of CoPc, CoPc-SO_3H, CNT, CoPc/CNT, and CoPc-SO_3H/CNT in O_2-saturated 1 M KOH at 10 mV s^{-1}. d, e) Reproduced with permission from Ref. [116]. Copyright 2019, The Royal Society of Chemistry.

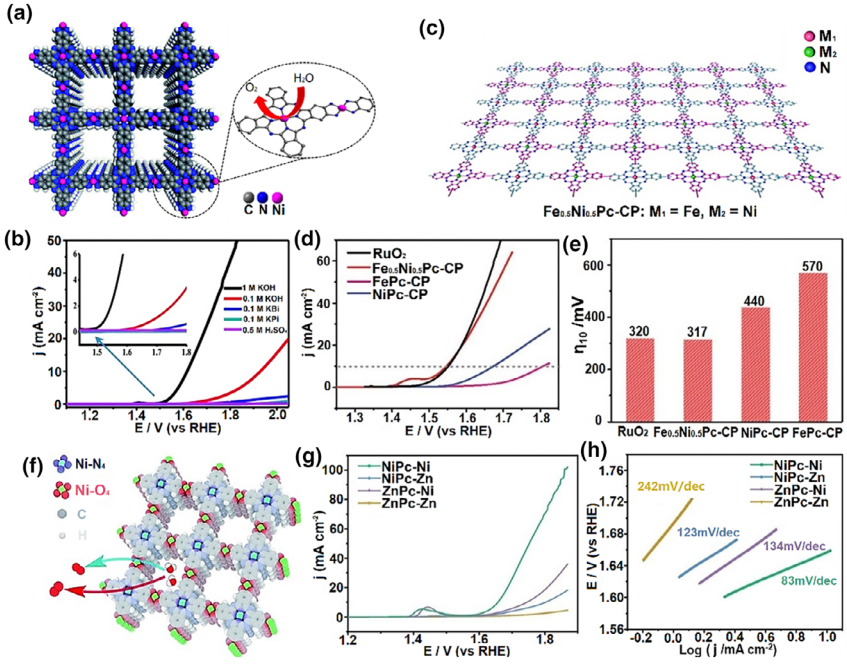

Figure 14. 2D conjugated MPc materials for OER. a) Structural diagram of the NiPc–MOF and its chemical structure. b) The pH-dependent LSV curves using the NiPc–MOF as the OER catalyst. a–b) Reproduced with permission from Ref. [117]. Copyright 2018, The Royal Society of Chemistry. c) Schematic illustration of as-synthesized $Fe_{0.5}Ni_{0.5}$Pc-CP. d) LSV curves and e) overpotential at 10 mA cm^{-2} of $Fe_{0.5}Ni_{0.5}$Pc-CP, FePc-CP, NiPc-CP, and RuO_2 in 1.0 M KOH solution. c–e) Reproduced with permission from Ref. [118]. Copyright 2020, The Royal Society of Chemistry. f) Schematic illustration of Ni–O_4 and Ni–N_4 sites in NiPc–Ni. g) LSV curves and h) Tafel plots for NiPc–Ni, NiPc–Zn, ZnPc–Ni, and ZnPc–Zn in 1.0 M KOH. Reproduced with permission from Ref. [120]. f–h) Copyright 2021, The Royal Society of Chemistry.

conductive bimetallic MPc-M' (M=Ni, Zn) MOF toward OER in 1.0 M KOH solution (Figure 14f).[120] DFT calculations revealed that the optimized NiPc–Ni MOF has a narrow band gap and excellent conductivity. The experimental results suggested that the synergistic modulation of electronic structure between Ni–O_4 and Ni–N_4 dual sites improves the intrinsic OER activity, thus exhibiting a lower overpotential compared to the NiPc–Zn, ZnPc–Ni, and ZnPc–Zn MOF (Figure 14g,h). Furthermore, the introduction of additional metal atoms moves the metal d-band center to a higher energy (closer to the Fermi level) effectively adjusting the electron distribution of the conjugated structure, which is closely related to the adsorption strength of the relevant intermediates at the active site. The modulation strategy on the electronic structure of the Ni–O_4 site doped with a certain amount of Fe in conductive MOFs is deemed to enhance the oxygen evolution activity.[121] As expected, the electronic interaction between the Ni–O_4 and Fe–O_4 centers heightened their intrinsic catalytic activity. The optimized NiPc–$NiFe_{0.09}$ displayed a low overpotential and an ultrahigh turnover frequency (TOF) value. Such atom-scale modulations on MPc-based materials enable the high catalytic activity to exceed those of most noble metal catalysts.

4.3. HER

4.3.1. Equation and Mechanism of Electrocatalytic HER

HER, the cathodic half-reaction of water electrolysis, is an ideal strategy for realizing clean and efficient hydrogen energy, which is perceived as a cost-effective and broad avenue.[122,123] Theoretical calculations of the $2e^-$ transfer reaction pathway revealed that the overall reaction rate of HER is chiefly dependent on the Gibbs free energy of hydrogen adsorption (ΔG_H), which is crucial for measuring the hydrogen evolution activity.[124] The Volmer process-involved HER is the adsorption of hydrogen-containing compounds at catalytic active sites with MPcs, resulting in forming catalytic intermediates. It is carried out by the dissociation of H_3O^+ and H_2O in acidic and alkaline media, respectively. The second step is the formation of H_2 molecules, which are divided into two main reaction pathways. In the Heyrovsky step, the catalyst adsorbate undergoes secondary electron transfer, which is then desorbed from the active units. In contrast, the self-linking coupling of the intermediates forms the Tafel step.

Therefore, the entire HER process can be categorized as the Volmer–Heyrovsky mechanism and Volmer–Tafel counterpart for MPc-based catalysts, and the equations are as follows.[90] The smaller Tafel slope affects the reaction kinetics and can be utilized to judge the RDS of the reaction along with the mechanism.

$$\text{Volmer step}: M + H^+ + e^- \rightarrow M{-}H \quad (1)$$

$$M + H_2O + e^- \rightarrow M{-}H + OH^- \quad (2)$$

$$\text{Heyrovsky step}: M{-}H + H^+ + e^- \rightarrow M + H_2 \quad (3)$$

$$M{-}H + H_2O + e^- \rightarrow M + H_2 + OH^- \quad (4)$$

$$\text{Tafel step}: M{-}H \rightarrow M + 1/2H_2 \quad (5)$$

4.3.2. HER Electrocatalysts of MPc-Based Structure

Among the various catalysts, macrocyclic MPcs are considered as one kind of promising HER catalysts with ΔG_H close to 0 except for the Pt criterion. The diverse coordination types of MPcs benefit from the highly tunable molecular structure, which makes it easier to form a hyperbranched configuration. In the synthesis process, SiO_2 nanospheres are often used as templates to prepare hyperbranched covalent organometallic polymers with large porosity and uniform mesoporous structure. Also, increasing the specific surface area is beneficial to expose more active parts. The bonding mode of atoms also plays a crucial part in tuning the electrocatalytic activity of nanohybrid materials. In 2019, Wang et al. reported two constituent-tunable metal–organic polymers ZnPc-COPs, which were covalently linked to GO with –CO–NH– as the linking unit (GO-PcP 1 and GO-PcP 2) applied in HER process in 0.5 M H_2SO_4 solution.[125] The two materials linked by different phthalocyanine-branched chains showed low overpotentials of 237 and 210 mV, respectively, which can be ascribed to unique microstructures of the two branched precursors facilitating charge transmission and conductivity. This also indicated that the conjugated polymerization systems of MPcs significantly increase the catalytic activity of the reduction reaction and stability in an acidic environment.

In addition, the unique 2D structure enables coupling with other metal ion moieties on the surface to build an electrocatalytic composite. Based on this, Zhang et al. developed FePc-anchored 2D ultrathin Ni-MOF nanosheets (denoted as FePc@Ni-MOF) through an ultrasonic treatment-assisted one-pot reaction.[63] Particularly, 2D Ni-BDC nanosheets constructed by joining nickel ions with BDC ligands possess coordinatively unsaturated metal sites and dangling bonds. The precise localization of the interaction between FePc and the strong π–π sheet stacking of the Ni-based framework promotes the fast electron transfer toward HER, which adjusts the electronic environment of Fe and Ni at the active site, resulting in enhanced HER performance. The increased active surface area of FePc@Ni-MOF nanosheets is beneficial to more active sites accessible. In previous studies, Monama et al. developed palladium-supported CuPc/MOF composites with significantly improved electrochemical hydrogen evolution performance.[126] Afterward, they also prepared a novel hybrid nanocomposite based on 4-tetranitro copper phthalocyanine (TNCuPc) grown on MOFs as noble metal-free HER catalysts via a mild impregnation method.[127] Compared with bare MOF and TNCuPc, the TNCuPc/MOF composites showed more negative potential shifts in the HER wave. The resulting positive role may be ascribed to the synergistic effect of MOF and TNCuPc. Despite the widespread popularity of MPc porous materials in energy conversion systems in recent years, their applications toward HER were still seldom reported. A comparison of the electrocatalytic performance parameters for MPc-based electrocatalysts is shown in detail in **Table 2**, including ORR, OER, and HER.

4.4. CO_2RR

4.4.1. Mechanism of Electrocatalytic CO_2RR

Owing to the growing concentration of the greenhouse gas CO_2 causing a series of ecological and environmental problems, CO_2RR by carbon fixation into high value-added profitable organics is another significative choice, which is one of the hot topics in frontier research.[127–130] In the CO_2RR, the binding energy between the active surface of the catalysts and the reaction intermediates restricts the electron transfer in the reduction process.[131] For MPc-based catalysts, during CO_2 molecules combining with different H^+/e^- on the C/O atom, a set of diverse carbon-rich organisms can be formed (**Figure 15a**).[91,132] It has been confirmed that M–OCHO is a more efficient intermediate than M–COOH in the evolution of formate.[132,133] However, generally, the electrochemical reduction of CO_2 to CO is accomplished through the intermediate product M–COOH, which has been reported.[134] The formation of M–COOH can be achieved by the electron transfer process of CO_2 molecule coupling with proton H^+. The equilibrium potentials of the majority of CO_2 reduction half-reactions are close to 0 V, which overlapped with practical HER potential windows making the occurrence of side reactions seriously affecting the CO_2RR Faradaic efficiency. Generally, efficient MPc-based catalysts toward CO_2-to-CO require a strong binding energy of *COOH (E_b^{*COOH}) and a weak binding energy of *CO (E_b^{*CO}) at metal sites, which is usually accompanied by a linear relationship (Figure 15b).[135]

In the MPc structure, the metal active centers play an important role in the regulation of the binding energy toward *COOH, *H, and *CO. Therefore, various MPc centered on d-block metals have been obtained and applied to electrocatalytic CO_2RR, especially FePc and NiPc were identified as efficient candidates for CO production.[136] MPcs can exhibit high selectivity and activity by controlling the oxidation states of metal ions. For example, FePc can display unusual redox pair M(I)/M(0) in the voltage range of cathodic CO_2 reduction, generated Fe(0)Pc species can easily transfer the electron from HOMO-orbital into LUMO-orbital to absorb CO_2 molecules to form Fe(I)Pc–CO_2 additions. However, the electron transfer of Fe(II)/Fe(0) redox pair may lead to an increase in the radius of Fe ion at the central site, and strong inversion interaction of CO adsorption at Fe–N moieties increases the length of Fe–N bond, further leading to the removal of Fe from the Pc framework.[53] In contrast, M(II)/M(I) redox pairs at metal sites in NiPc, can exhibit weak CO binding affinity, leading to excellent CO_2RR activity. Therefore, it is important to select suitable MPc materials and adjust the surface binding properties accordingly to improve CO_2 reduction activity.

4.4.2. CO_2RR Catalysts of MPc-Based Structure

Modulating the molecular expression behavior by the construction of heterogeneous catalysts is effective to overcome the kinetic hindrance of CO_2 reduction. Meanwhile, the adjustment of molecule-coupled

Table 2. Electrocatalytic performance of the advanced MPc-based catalysts toward OER, HER, and ORR.

Catalysts		Application	Electrolyte	Potential (V vs. RHE)	Tafel slope (mV dec^{-1})	Stability	References
MPc composites	Fe-PyNGs	ORR	0.1 M KOH	E_{onset} = 0.969	—	91.3% mA cm^{-2} after 5000 cycles CV	[101]
	FeAB-O	ORR	0.1 M KOH	$E_{1/2}$ = 0.900	27.5	99.2% mA cm^{-2} after 10 000 s i-*t* test	[102]
	FePc-MoS_2	ORR	0.1 M KOH	$E_{1/2}$ = 0.890	35	A current loss of 9.3% after 20 h i-*t* test	[62]
		HER	0.5 M H_2SO_4	η = 0.123 V @ 10 mA cm^{-2}	32	—	
	TACoPc + IrO_2/Ni	OER	1.0 M KOH	η = 0.304 @ 10 mA cm^{-2}	38	A constant overpotential at least 9 h	[115]
	CoPc-SO_3H/CNT	ORR	0.1 M KOH	E_{onset} = 0.880	41	—	[116]
		OER	1.0 M KOH	η = 0.390 @ 10 mA cm^{-2}	48	A slight loss after 1000 cycles CV	
Conjugated MPcs	FePPc-$(COOH)_2$/C	ORR	0.1 M $HClO_4$	$E_{1/2}$ = 0.800	—	83% mA cm^{-2} after i-*t* test	[92]
	FePPc@CB	ORR	0.1 M KOH	$E_{1/2}$ = 0.908	29	73% mA cm^{-2} after 40 000 s i-*t* test	[105]
	PFePc-I/C	ORR	0.1 M KOH	$E_{1/2}$ = 0.948	36.6	98.1% mA cm^{-2} after 20 000 cycles CV	[104]
	CPMPcFe/C	ORR	0.1 M KOH	E_{onset} = 1.000 $E_{1/2}$ = 0.870	68.5	A small activity loss of 0.05 mA cm^{-2} after 5000 cycles CV	[106]
	PcCu-O_8-Co/CNT	ORR	0.1 M KOH	E_{onset} = 0.820 $E_{1/2}$ = 0.830	61	Little changes of $E_{1/2}$ (16 mV) after 5000 cycles CV	[103]
	CAN-Pc(Fe/Co)	ORR	0.1 M KOH	E_{onset} = 1.040 $E_{1/2}$ = 0.840	54	74.6% mA cm^{-2} after 12 000 s i-*t* test	[108]
	CAN-Pc(Co)-p	ORR	0.1 M KOH	E_{onset} = 1.050 $E_{1/2}$ = 0.850	40	87.6% mA cm^{-2} after 12 000 s i-*t* test	[76]
	Co-PyPc NSs	ORR	0.1 M KOH	E_{onset} = 0.974 $E_{1/2}$ = 0.815	—	—	[81]
	$Fe_{0.5}Co_{0.5}$Pc-CPs	ORR	0.1 M KOH	E_{onset} = 0.937	—	—	[77]
	$Fe_{0.5}Co_{0.5}$Pc-CP NS@G			$E_{1/2}$ = 0.848 E_{onset} = 1.006 $E_{1/2}$ = 0.927	—	81.7% mA cm^{-2} after 20 000 s i-*t* test	
	NiPc–MOF	OER	1.0 M KOH	η = 350 @ 10 mA cm^{-2}	74	An almost constant at ~1.50 V for 50 h	[117]
	$Fe_{0.5}Ni_{0.5}$Pc-CP	OER	1.0 M KOH	η = 0.317 @ 10 mA cm^{-2}	116	85% $mAcm^{-2}$ after 10 000 s i-*t* test	[118]
	CPF-Fe/Ni	OER	0.5 M H_2SO_4	η = 0.042 @ 10 mA cm^{-2}	82.6	A nearly constant at 200 h i-*t* test	[119]
			1.0 M KOH	η = 0.194 @ 10 mA cm^{-2}	94.1	A nearly constant at 200 h i-*t* test	
	NiPc-Ni MOF	OER	1.0 M KOH	η = 0.319 @ 10 mA cm^{-2}	83	A nearly constant after 12 h i-*t* test	[120]
	NiPc-$NiFe_{0.09}$ MOF	OER	1.0 M KOH	η = 0.300 @ 10 mA cm^{-2}	55	A slight positive shift (33 mV shift at 50 mA cm^{-2}) after 1000 cycles	[121]
	FePc@Ni-MOF	HER	0.1 M KOH	η = 0.334 @ 10 mA cm^{-2}	72	A slight loss after 1000 cycles CV	[63]

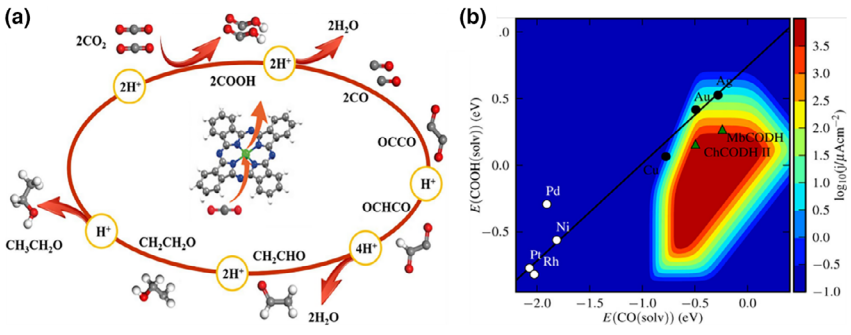

Figure 15. a) Possible CO_2RR mechanisms catalyzed by MPcs. Reproduced with permission from Ref. [91]. Copyright 2020, Elsevier B.V. b) A LSR of binding energy E_b^{*COOH} versus E_b^{*CO} on transition metals. Reproduced with permission from Ref. [91]. Copyright 2021, American Chemical Society.

heterogeneous atomic substrates can avoid the aggregation of macrocyclic molecules and thus improve the electron transport capacity to obtain enhanced reduction efficiency. In general, the dominant transition metals with 3d orbits in the MPcs become the catalytic active center for multiple proton-coupled electron transfer toward the CO_2 reduction process. The CO_2 conversion into CO occurs with minimal energy replenishment. To improve the CO_2-to-CO reduction efficiency of the electrocatalysts, both the Ni–N_4 active sites in the metal macrocyclic NiPc and the surface pyridine defective N-doping in the carbon matrix are put forward to form the Ni–N_5 component structure, synergistically promoting the reduction

reaction (**Figure 16a**).[137] It was experimentally measured that the reduction Faraday efficiency (FE) can reach up to 98% at a potential of −0.5 V (Figure 16b,c). The NiPc@pyridine N surface solely requires a lower potential barrier (+0.89 eV), which is more likely to occur than NiPc@graphitic N, NiPc@pyrrolic N, and NiPc@C as supported by DFT (Figure 16d).[137,138] The high-spin Ni 3d orbital-rich unpaired electrons have a strong CO_2 affinity, and the metal center as the reactive site is beneficial to the formation of key intermediates and enhances the CO_2 reduction rate. Additionally, Co(II)-2,3-naphthalocyanine (NapCo) complexes covalently grafted on graphene sheets with rich heteroatom groups (–S=O, –COOH) have also been reported (Figure 16e).[139] The stacking of axial coordination between CoPc macrocycle and the function-doped graphene promotes a strong π–π conjugated system and the regulation of electron cloud density significantly improved the catalytic performance of CO_2RR through Co–O as the major linking site. NapCo@SNG (SNG = S/N/O heteroatoms doped graphene) compound derived a higher selectivity for CO_2RR at −0.8 V and a FE_{CO} of ∼97% (Figure 16f), which is ascribed to the introduction of sulfoxide dopant promoting the electron transport effect of axial coordination.

Compared with solid-phase metal catalysts, functional mesh-like porous COFs and MOFs with designable organic unit connectors exhibit excellent reduction efficiency and high selectivity toward CO_2RR owing to their accessible precise active sites and strong CO_2 adsorption. It is found that the porous structure of Co-based COF has a competitive advantage in CO_2 storage, maintaining a high CO_2 concentration near the active site of the reduction center.[140] This also enables both the CO_2 mass transfer performance and CO_2 reduction yield to be significantly improved. Wu et al. first designed a CoPc polymer backbone with a special structure to promote the slow CO_2RR by an introduction of defective sites into the transition metal macrocyclic network.[45] The prepared D-P-CoPc showed high reduction properties, exhibiting a FE of ∼97%. An overpotential as low as 490 mV can maintain long-standing stability. In 2020, substituted octahydroxyphthalocyanines and octaaminophthalocyanines based on two organic monomer building blocks were assembled into 2D COFs via a molecular bridge, providing two strongly functional 2D COFs CO_2RR electrocatalysts.[141-143] In this regard, 2D polyimide-linked phthalocyanine COFs, CoPc-PI-COF-1 and CoPc-PI-COF-2, have been devised and prepared (Figure 16g).[144] The higher CO_2 reduction ability could be attributed to facilitated charge transportation to achieve stronger electrical conductivity than CoPc-PI-COF-2 (Figure 16h). Therefore, CoPc-PI-COF-1 cathode composition displayed a similar FE_{CO} of 87%–97% between −0.60 and −0.90 V (Figure 16i). In addition, Yi et al. prepared conductive 2D phthalocyanine-based MOF nanosheets (NiPc–NiO_4) linked by nickel catechol as an efficient electrocatalyst for the conversion of CO_2 to CO.[80] Due to the exposure of more Ni sites of thin lamellar, the fabricated nanosheets have an ultrahigh selectivity.

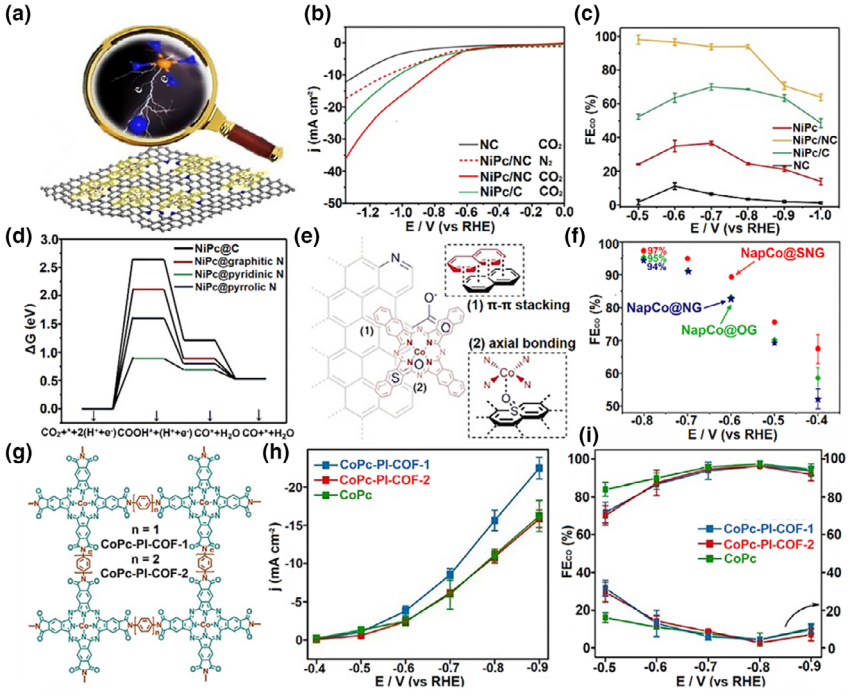

Figure 16. MPc materials toward CO_2 to CO reactions. a) Schematic illustration of NiPc/NC catalyst. b) LSV curves in an N_2-saturated or CO_2-saturated 0.5 M $KHCO_3$ electrolyte at a scan rate of 50 mV s^{-1}. c) FEs of CO of the NC, NiPc, NiPc/C, and NiPc/NC catalysts at different applied potentials. d) Calculated free energy diagrams for CO_2RR to CO on different catalysts. a–d) Reproduced with permission from Ref. [137]. Copyright 2020, American Chemical Society. e) Schematic illustration of NapCo onto doped graphene heterogenization through π–π stacking and coordination with heteroatoms. f) FEs of CO_2RR on NapCo@SNG/NG/OG in CO_2-saturated 0.1 M $KHCO_3$. e, f) Reproduced with permission from Ref. [139]. Copyright 2019, Wiley-VCH Verlag GmbH & Co. KGaA, Weinheim. g) Structural illustration of as-synthesized CoPc-PI-COF-1 and CoPc-PI-COF-2. h) Partial CO current density and i) FE_{CO} of CoPc-PI-COF-1, CoPc-PI-COF-2, and CoPc. g–i) Reproduced with permission from Ref. [142]. Copyright 2021, American Chemical Society.

During CO_2 conversion process, due to the high overpotential and less electron transfer compared with other reduction species, the reduction products CO and formic acid account for the majority, while the hydrocarbons are less. In practice, the multicarbon compounds are expected to be yielded because of the higher industrial values. Until now, Cu-based compounds have been considered the major materials catalyzing CO_2 to carbon-rich products. However, the low selectivity and FE of C_{2+} reduction products involved in copper-based catalysts are still major problems that cannot meet the needs of large-scale commercialization. MPcs complexes are effective for CO_2RR. Weng et al. demonstrated initially that CuPc possessed the highest activity for methane with a FE of 66% delivering a partial current density of 13 mA cm^{-2} at a potential of −1.06 V.[145] Under operating conditions, it underwent reversible structural changes to form metallic copper clusters with the ability to catalyze the conversion of CO_2 to methane. Therefore, it is found that the recombination inducing strategy provided an opportunity for the design of efficient electrocatalysts. For CO_2RR, CuPc catalysts still have much to explore. To further address the shortcomings of the high energy barrier and thus enhance the CO_2 reduction efficiency, encapsulation of MPc compounds as a secondary structural unit into highly ordered framework COFs and MOFs of tetragonal network π-conjugated structures was proposed, with advantages of well-defined catalytic active centers and structural designability. Qiu et al. developed

a PcCu–Cu–O MOF catalyst composed of PcCu–$(OH)_8$ ligands and square planar CuO_4 nodes for the CO_2 reduction to C_2H_4 (**Figure 17a**).[146] The PcCu–Cu–O MOF exhibited superior electrocatalytic reduction behavior for the production of C_2H_4, which is attributed to the coupling of dual active sites, and in situ attenuated total reflection Fourier transform infrared (ATR-FTIR) measurements well validated this mechanism (Figure 17b,c). The generated CO on the CuO_4 site can efficiently migrate and dimerize with the *CO intermediate adsorbed on the CuPc site for C_2H_4 products, resulting in reducing the C–C dimerization energy barrier trend, as depicted in Figure 17d. In addition, it is desirable to produce high value-added product acetate by CO_2 reduction. The major problem is that the selectivity of acetate is often lower than those of ethylene and ethanol. The choice of materials compatible with theoretical guidance is therefore the key to solving the problem. Previous mechanistic studies indicated that the conversion of CO_2 to acetate requires a C–C coupling of $*CH_3$ and CO_2, so COF materials with single or isolated M–N_4 active centers may be advantageous. In 2022, a stable PcCu-based 2D COF framework CuPc-TFPN (TFPN = 2,3,5,6-tetrafluoroterephthalonitrile) was designed for the selective conversion of CO_2 to acetate, and the results showed a high single-product FE of ~90% (Figure 17e,f).[147] Moreover, the robust PcCu-based COF can maintain its activity for a long-term operation (Figure 17g). An appropriate pathway is given for electrocatalytic CO_2 to acetate by assisted in situ ATR-FTIR (Figure 17h,i). The isolated CuPc active site with high electron density plays a key step in the C-C coupling of the $*CH_3$ intermediate with CO_2 to form acetate. Since PcCu-TFPN is a single active site electrocatalyst structure, *CO cannot be coupled with the immediately adjacent *CO or *CHO, avoiding the generation of ethylene and ethanol. The rational design of the crystalline structure and the involvement of the different active centers considerably affect the reaction pathway, which consequently improves the selectivity of acetate products.

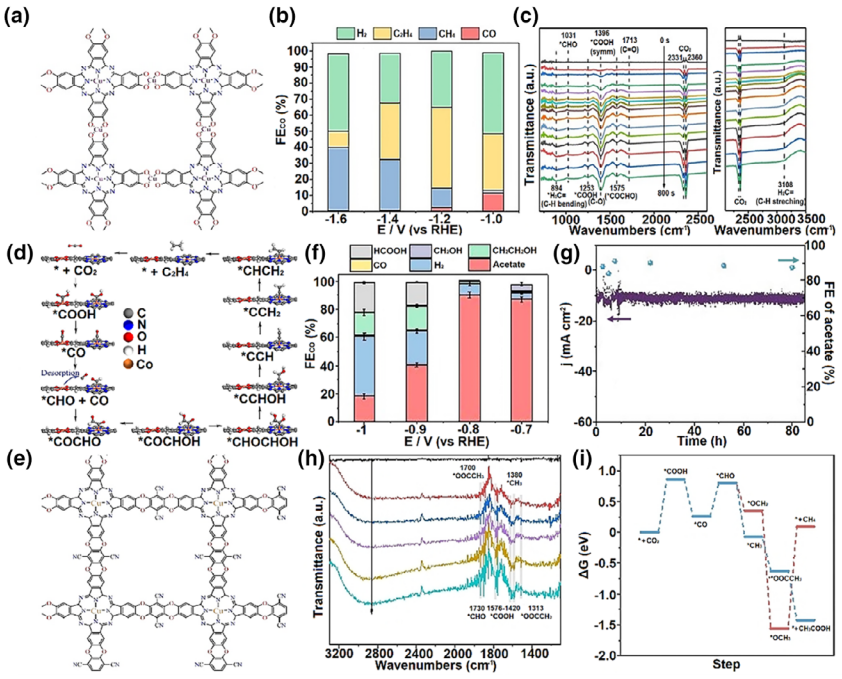

Figure 17. MPc materials for the reduction of CO_2 into multicarbon products. a) Illustration of the structure of PcCu-Cu-O. b) In situ ATR-FTIR spectra of PcCu-Cu-O during the electrochemical CO_2RR. c) FEs of C_2H_4, CH_4, CO, and H_2 for PcCu-Cu-O. d) Proposed CO_2RR mechanism of PcCu-Cu-O. a–d) Reproduced with permission from Ref. [144] Copyright 2021, American Chemical Society. e) Illustration of the structure of PcCu-TFPN. f) FEs of CO_2RR products under different voltages in 0.1 M $KHCO_3$ solution. g) Durability of PcCu-TFPN in the electrocatalysis at the potential of −0.8 V. h) In situ ATR-FTIR spectra of PcCu-TFPN during the electrocatalytic CO_2RR. i) Free energy diagrams of electrocatalytic reduction of CO_2 to acetate by PcCu-TFPN. e–i) Reproduced with permission from Ref. [145]. Copyright 2022, Wiley-VCH GmbH.

4.5. NRR

4.5.1. Mechanism of Electrocatalytic NRR

Electrochemical ammonia synthesis, an important feasible way to replace the traditional Haber–Bosch process that utilizes industrial fossil fuels to produce ammonia with high-energy consumption, has attracted an amount of research interest.[148,149] The green and sustainable electrochemical NRR processes ($N_2 + 6H^+ + 6e^- \rightarrow 2NH_3$ and/or $N_2 + 6H_2O + 6e^- \rightarrow 2NH_3 + 6OH^-$) can be carried out under room temperature conditions using reproducible electricity resource, offering the possibility for its extensive industrialization under mild conditions in the future.

The low solubility of N_2 in water at normal temperature and pressure and the limitation of the mass transfer diffusion process may affect the overall reaction efficiency. The hydrogenation activation process of N_2 is critical in the whole reaction. The dissociative mechanism occurs in the industrial Haber–Bosch process in which adsorbed N* is hydrogenated in turn to form NH_3, and then desorbed from the surface. It is shown that MPc-based materials are considered active and efficient NRR electrocatalysts due to isolated and highly exposed metal active sites. For MPc catalysts, there are four possible mechanisms of adsorption activation on the most promising, namely, distal coordination mechanism, alternating coordination mechanism, enzymatic process, and mixed mechanism (**Figure 18**).[150,151] Owing to the inherently high N≡N bond energy (941 kJ mol^{-1}), N_2 molecules are rather stable that both the activation and cleavage of chemical bonds are arduous. Therefore, the hydrogenation reduction process is often identified as the possible RDS in different mechanisms. On the other hand, in terms of both thermodynamic equilibrium and kinetics, the competitive HER with similar reaction potential affecting the NRR efficiency also exists.[152] The adsorption energy of N atoms is also an important factor influencing the catalytic performance. For example, moderate N* free energy is favorable for the surface desorption of ammonia.[153]

4.5.2. NRR Catalysts of MPc-Based Structure

The impediment and low selectivity of electrocatalytic NRR suffering from the high energy barrier of N_2 activation and the faster kinetics of the

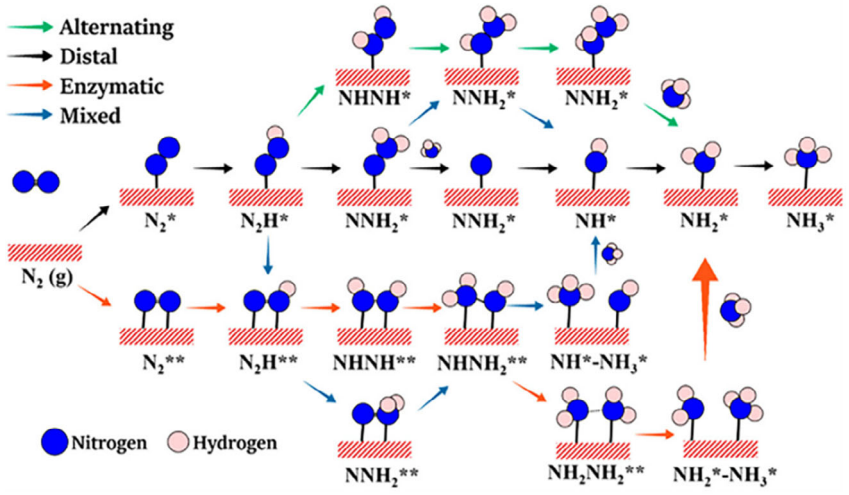

Figure 18. Schematic illustration of the possible reaction mechanisms toward NRR reduction. Reproduced with permission from Ref. [151]. Copyright 2020, American Chemical Society.

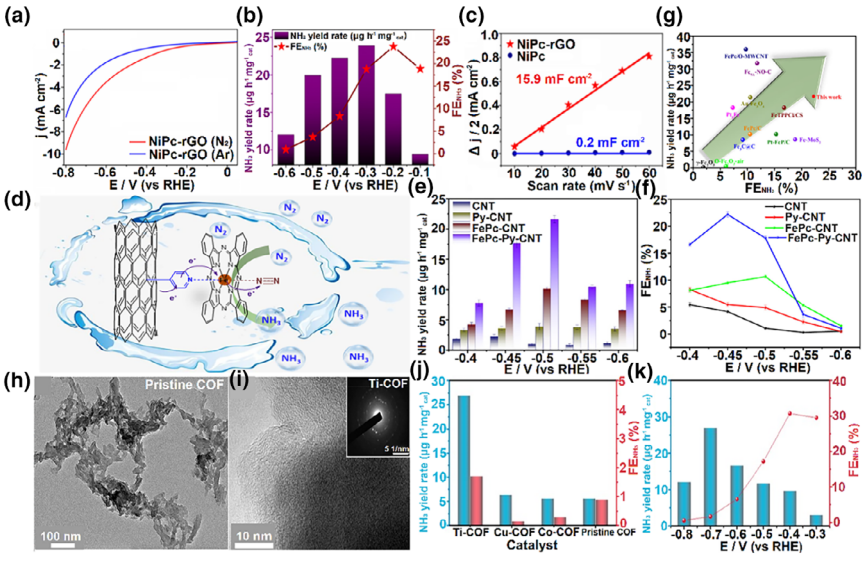

Figure 19. MPc materials for NRR. a) LSV curves of NiPc-rGO in Ar and N_2 saturated 0.1 M HCl solution. b) FE and NH_3 yield rates of at various potentials. c) Plots of current density differences ($\Delta j/2$) versus scan rate at −0.15 V and C_{dl} values for NiPc and NiPc–rGO. a–c) Reproduced with permission from Ref. [156]. Copyright 2022, Elsevier B.V. d) Illustration of the structure of FePc-Py-CNT toward NRR to NH_3. e) NH_3 yields and f) FEs of FePc-Py-CNT, FePc-CNT, Py-CNT, and CNT at different potentials. g) FE values and NH_3 yield rates of FePc-Py-CNT compared with other recently reported Fe-based catalysts. d–g) Reproduced with permission from Ref. [157]. Copyright 2022, American Chemical Society. h) TEM image of pristine COF. i) HRTEM, and *inset* SAED images of Ti-COF. j) Comparison of NH_3 yields and FE values of different catalysts measured at −0.7 V in 0.05 M HCl solution. k) Yield rate of NH_3 and FE of Ti-COF at given potentials in N_2-saturated 0.05 M HCl electrolyte. h–k) Reproduced with permission from Ref. [158]. Copyright 2021, American Chemical Society.

competing HER make it desirable to develop high-efficiency electrocatalysts.[154,155] Therefore, it is necessary to strategically tailor an efficient nitrogen fixation catalyst to maximize ammonia production, achieving the purpose of improving the catalytic activity of the reaction. Shyamal Murmu et al. developed a graphene-coated NiPc nanohybrid (NiPc-rGO) for electrocatalytic ammonia generation reaction.[156] It showed a maximum ammonia yield of 23.9 $\mu g\,h^{-1}\,mg^{-1}_{cat}$ at −0.3 V, while the highest FE of 23.8% was obtained at −0.2 V (**Figure 19a,b**). The increased double-layer capacitance (C_{dl}) of NiPc-rGO compared to that of NiPc is shown in Figure 19c. It indicated that the nanohybrid exposed more active surface than NiPc while having high specificity for ammonia synthesis, thus NiPc-rGO showed higher NRR activity. Furthermore, by introducing an axial coordination group, a well-organized electrocatalyst (FePc-Py-CNT) can be formed by homogeneously immobilizing FePc on pyridine-functionalized CNT (Figure 19d).[157] The resulting hybrids exhibited significantly enhanced electrocatalytic NRR performance compared to FePc immobilized on bare CNT (FePc-CNT) based on π–π stacking, leading to a doubled NH_3 yield (21.7 $\mu g\,h^{-1}\,mg^{-1}_{cat}$) and Faradaic efficiency (22.2%) (Figure 19e–g). The axial interaction on FePc led to the evolution of partial electron density, which effectively suppressed the active intensity of H* and enhanced N_2 chemisorption at the active sites. This work provided new inspiration for the viable design of NRR advanced electrocatalysts at the molecular level.

Nonetheless, it is conjectured to covalently associate COFs with transition metals by organic molecules, which may provide more opportunities for designing catalysts with abundant active sites. Jiang et al. proposed a general pyrolysis-free synthesis method to prepare conjugated 2D COFs (Ti, Cu, Co–COF) with three intercalated transition metal central atoms and pristine non-nuclear COF (Figure 19h,i).[158] The Ti-assembled conjugated COF displayed the highest NRR catalytic activity and selectivity with an NH_3 yield of 26.89 $\mu g\cdot h^{-1}\,mg^{-1}_{cat}$ and an impressive FE of 34.62% (Figure 19j,k). Considering that the enhanced positive charge distribution of Ti atoms possessing strong adsorption with N atoms diminishes the energy barrier, therefore Ti-MOF shows a favorable activation of intermediates with a superior ability to suppress bad behaviors.

4.6. Photo-Assisted Electrocatalysis on MPcs

According to their molecular structure, MPcs have special light-absorbing properties, endowing them with huge potential in photocatalysis and photo-assisted electrocatalysts. Typically, in CO_2RR, the combination of the light field effect is beneficial to fully exploit the superiority of the material, overcoming the low activity and selectivity driven by electrical energy to exhibit improved electrocatalytic conversion efficiency.[157–161] MPc-based encapsulation crystalline materials are considered to be

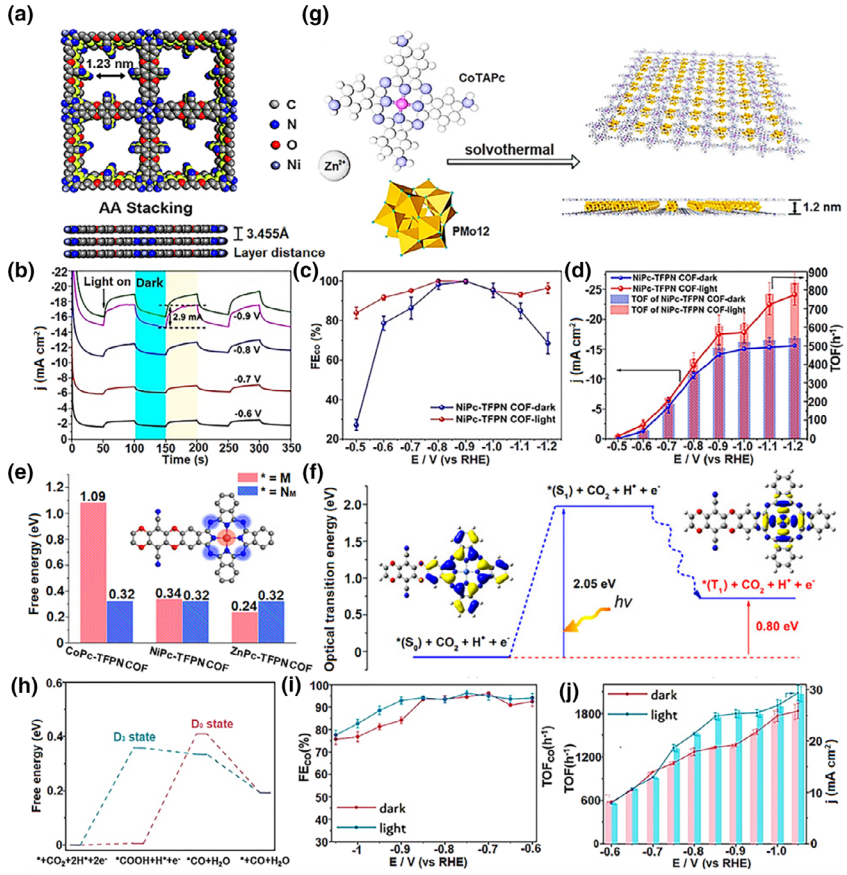

Figure 20. MPc materials for photo-assisted electrocatalysis reactions. a) Top view and side view of simulated AA stacking mode for NiPc-TFPN COF crystal structure. b) Photo-current response curve of NiPc-TFPN COF at different bias voltages. c) FE_{CO} and d) j_{CO} and TOF of NiPc-TFPN COF under dark and light in 0.5 M $KHCO_3$ solution. e) Comparison of the relative adsorption energy for the first step of CO_2RR on MPc-TFPN COF. f) Schematic representation of the excited states of NiPc-TFPN COF. a–f) Reproduced with permission from Ref. [142]. Copyright 2020, Wiley-VCH. g) Schematic illustration of synthetic procedure toward Zn-CoTAPc/PMo12 MLSs. h) Gibbs free energy diagram of CO_2RR pathway of Zn-CoTAPc/PMo12 MLSs. i) FE_{CO}-potential plots, j) j_{CO} and TOF_{CO} plots of Zn-CoTAPc/PMo12 MLSs in dark and light conditions. g–j) Reproduced with permission from Ref. [162]. Copyright 2021, American Chemical Society.

photosensitizers whose electronic structure properties can be significantly altered under the action of photoelectricity, thereby accelerating the transfer rate of charge carriers and the efficiency of CO_2 electrocatalytic reduction.[158–160] To investigate the electrocatalytic CO_2 reduction under photoelectric action, Lu et al. designed a series of dioxin-linked Pc-based 2D COFs with different metal centers (MPc-TFPN COF, M=Ni, Co, Zn) for the first time, particularly, NiPc-TFPN COFs can reach the highest CO_2-to-CO reduction FE of ~99% at −0.9 V (**Figure 20a**).[142] More importantly, compared with that in the dark environment, the CO_2 reduction performance of NiPc-TFPN COFs is further improved under illumination (Figure 20b), evidencing photoexcitation can indeed promote the CO_2 reduction activation behavior and thus improve the catalytic efficiency (Figure 20c,d). DFT calculations, as shown in Figure 20e, further show that CO_2 molecules tend to be adsorbed and activated on N sites of central metal for the first step of CO_2RR (i.e., RDS). Also, when electrons are excited to higher excited states, the transfer of electrons from ligands to active centers not only is enhanced, but also both the formation of active intermediates *COOH and the ability of electrochemically activating CO_2 are promoted (Figure 20f), indicating that light-energy coupling plays an important role in the electrocatalytic process. In addition, the presence of intercalated structures was regarded to allow for more accessibility of active sites from changing the aggregation of MPcs, which further stimulated enhanced activity. Moreover, Yang et al. developed a robust and stable interlayer phosphomolybdate-doped zinc-cobalt (tetraamino)phthalocyanine molecular layer sandwich nanosheets (Zn-CoTAPc/PMo12 MLSs) toward CO_2 reduction (Figure 20g).[162] The polyoxometalate (POM) anions sandwich support architectures are more conducive to the separation and transport ability of charge carriers during the photo-electrocatalytic CO_2 reduction process and ensure that the molecular layer obtains a larger current density. Under photo-assistance, the j_{CO} increased gradually, meaning that photons will affect the action behavior of the electron conduction band to CO_2 molecule, thereby improving its reduction performance (Figure 20h–j). On the other hand, in the optical field, the excited state electrons greatly suppressed the competitive HER, leading to a higher FE_{CO}. The realization of this structure also provided conditions for more extensive construction of MPc-MOF systems. **Table 3** shows the electrocatalytic performance of reported catalysts toward CO_2RR and NRR.

5. Conclusion and Perspectives

In summary, the recent research progress in the development and application of 2D MPc composites and conjugated organic frameworks (COFs and MOFs) as high-performance catalysts toward a variety of electrocatalytic and photocatalytic reactions is summarized. In addition, the structural properties and preparation strategies of MPc crystals are also reviewed. The topology of the structures can be achieved by the rational design of molecules and functional modifications, which can tune the physicochemical features of materials. In particular, the structural evolution from bulk to nanosheets is also mentioned. The excellent performance of thin-layered nanosheets opened a new platform to overcome the intrinsic insulating properties. Also, this work may provide new insights into the controllable preparation and structure–effect relationships of MPcs materials.

Although possessing excellent catalytic properties, macrocyclic MPcs, are still confronted with serious challenges and need to be further explored in the future, the research of MPcs as well as their derivatives may be concentrated on the following aspects:

i 2D COFs and MOFs-based materials assembled by MPc molecules have become a hot research topic in recent years. In particular, the electrocatalytic performance of MPc-based network polymer ultrathin nanosheet-like heterogeneous catalysts should be appreciated, which paves the way for the development of MPc-based materials

Table 3. Electrocatalytic performance of the MPc-based catalysts toward CO_2RR and NRR.

Catalysts		Applications	Electrolyte	Current density/yield	FE	Stability	References
MPc composites	NiPc/NC	$CO_2 \rightarrow CO$	0.5 M $KHCO_3$	35.9 mA·cm^{-2} @ −1.35 V	98% @ −0.5 V	A stable current density and FE_{CO} decreased to 93% at −0.6 V after 7 h i-*t* test	[137]
	NapCo@SNG	$CO_2 \rightarrow CO$	0.1 M $KHCO_3$	—	97% @ −0.8 V	A negligible current change at −0.8 V after 9000 s i-*t* test	[139]
	NiPc-rGO	NRR	0.1 M KOH	23.9 μg h^{-1} mg$^{-1}_{cat}$ @ −0.3 V	23.8% @ −0.2 V	An almost 100% performance retention at −0.3 V after 5 cycles	[156]
	FePc-Py-CNT	NRR	0.1 M HCl	21.7 μg h^{-1} mg$^{-1}_{cat}$ @ −0.5 V	22.2% @ −0.45 V	A negligible attenuation of current density at −0.5 V after 50 h i-*t* test	[157]
Conjugated MPcs	D-P-CoPc	$CO_2 \rightarrow CO$	0.5 M $KHCO_3$	375 mA mg^{-1} @ −0.61 V	55% @ −0.43 V	A negligible activity loss and stable current density at −0.61 V over 20 h	[45]
	CoPc-PDQ-COF	$CO_2 \rightarrow CO$	0.5 M $KHCO_3$	—	96% @ −0.66 V	No significant loss of current density and FE_{CO} at −0.66 V over 24 h i-*t* test	[141]
	NiPc-TFPN COF	$CO_2 \rightarrow CO$	0.5 M $KHCO_3$	Dark 14.1 A g^{-1} @ −0.9 V	99.8% @ −0.9 V	No obvious current drop and large FE fluctuation at −0.90 V	[142]
				Light 17.5 A g^{-1} @ −0.9 V	100% @ −0.9 V	—	
	NiPc-COF NSs	$CO_2 \rightarrow CO$	0.5 M $KHCO_3$	35 mA cm^{-2} @ −1.1 V	99.1% @ −0.9 V	No obvious decrease of over 98% FE_{CO} for 10 h	[143]
	CoPc-PI-COF-1	$CO_2 \rightarrow CO$	0.5 M $KHCO_3$	−21.2 mA cm^{-2} @ −0.90 V	97% @ −0.80 V	91% FE_{CO} at −0.70 V after 40 h i-*t* test	[144]
	CoPc-PI-COF-2			16.6 mA cm^{-2} @ −0.90 V	96% @ −0.80 V	No significant current drop at −0.7 V after 1200 s i-*t* test	
	NiPc-NiO_4 NSs	$CO_2 \rightarrow CO$	0.5 M $KHCO_3$	34.5 mA cm^{-2} @ −1.2 V	98.4% @ −0.85 V	A decrease of current density of 0.8 mA cm^{-2} at −0.85 V	[80]
	PcCu-Cu-O MOF	$CO_2 \rightarrow C_2H_4$	0.1 M $KHCO_3$	7.3 mA cm^{-2} @ −1.2 V	50% @ −1.2 V	No significant degradation of current density for i-*t* test at −1.2 V at least 4 h	[146]
	PcCu-TFPN	$CO_2 \rightarrow$ acetate	0.1 M $KHCO_3$	12.5 mA cm^{-2} @ −0.8 V	90.3(2)% @ −0.8 V	A stable FE and regular current density fluctuations at −0.8 V for 80 h	[147]
	Ti-COF	NRR	0.05 M HCl	26.9 μg h^{-1} mg$^{-1}_{cat}$ @ −0.7 V	34.62% @ −0.4 V	—	[158]
	Zn-CoTAPc/ PMo12 MLSs	$CO_2 \rightarrow CO$	0.5 M $KHCO_3$	Dark —	96.1% @ −0.7 V	A stable current density and high FE_{CO} at −0.75 V after 12 h test	[163]
				Light —	96.2% @ −0.75 V		

in circuit systems such as fuel cells. In addition, integrating MPc-COFs with inorganic supports and/or MOF hybrid materials to construct efficient heterogeneous catalysts may be possible research direction in the near future.[163,164]

ii At present, although the mechanism of CPs electrocatalysis has been verified by theoretical calculations, it is still not enough to summarize the role in the reaction. Therefore, it is necessary to supplement it with advanced characterization technologies such as in situ observation for exploiting theoretical calculation research applied to COFs. What's more, the definition of more precise molecular descriptors should be provided as a guideline for the structural optimization and cycling stability of catalysts.

iii The highly reactive conjugated MPc building blocks facilitate the electrocatalytic reaction. Meanwhile, in the course of catalytic preparation and design, it is vital to concentrate on its durability to meet the needs of practical applications. However, the synergism between the activity and stability of MPc CPs catalysts is still at the research bottleneck stage and needs a breakthrough. The development of new structures is supposed to develop catalyst products with high activity and stability. For example, currently, some attention has been paid to the role of linkage chemistry in the active framework for both activity and stability aspects.[165] The introduction of specific functional chemical bonds may result in unexpectedly tunable and stable frameworks.

Acknowledgements

X.W. and S.S. worked equally to this work. This work is financially supported by the National Natural Science Foundation of China (51702291), the China Postdoctoral Science Foundation (2020M682352), and the State Key Laboratory of Powder Metallurgy, Central South University, Changsha, China. H.W. acknowledges support from the Project of Zhongyuan Critical Metals Laboratory (GJJSGFYQ202336) and the Youth Talent Program of Zhengzhou University (32340398).

Conflict of Interest

The authors declare that they have no known competing financial interests or personal relationships that could have appeared to influence the work reported in this article.

Keywords

conjugated nanostructure, electrocatalysis, 2D metallophthalocyanines

Received: August 14, 2023
Revised: November 27, 2023
Published online: November 29, 2023

[1] S. Chu, Y. Cui, N. Liu, *Nat. Mater.* **2017**, *16*, 16.
[2] N.-T. Suen, S.-F. Hung, Q. Quan, N. Zhang, Y.-J. Xu, H. M. Chen, *Chem. Soc. Rev.* **2017**, *46*, 337.
[3] Z. Yang, J. Zhang, M. C. W. Kintner-Meyer, X. Lu, D. Choi, J. P. Lemmon, J. Liu, *Chem. Rev.* **2011**, *111*, 3577.
[4] H. Wan, L. Hu, X. Liu, Y. Zhang, G. Chen, N. Zhang, R. Ma, *Chem. Sci.* **2023**, *14*, 2776.
[5] J. N. Hansen, H. Prats, K. K. Toudahl, N. Mørch Secher, K. Chan, J. Kibsgaard, I. Chorkendorff, *ACS Energy Lett.* **2021**, *6*, 1175.
[6] R. Venegas, K. Muñoz-Becerra, C. Candia-Onfray, J. F. Marco, J. H. Zagal, F. J. Recio, *Electrochim. Acta* **2020**, *332*, 135340.
[7] B. Chen, D. Chao, E. Liu, M. Jaroniec, N. Zhao, S.-Z. Qiao, *Energ. Environ. Sci.* **2020**, *13*, 1096.
[8] J. Pan, Y. Y. Xu, H. Yang, Z. Dong, H. Liu, B. Y. Xia, *Adv. Sci.* **2018**, *5*, 1700691.
[9] V. Aravindan, Y.-S. Lee, S. Madhavi, *Adv. Energy Mater.* **2015**, *5*, 1402225.
[10] R. G. Grim, Z. Huang, M. T. Guarnieri, J. R. Ferrell, L. Tao, J. A. Schaidle, *Energ. Environ. Sci.* **2020**, *13*, 472.
[11] J. H. Zagal, *Coord. Chem. Rev.* **1992**, *119*, 89.
[12] W. Liu, Y. Hou, H. Pan, W. Liu, D. Qi, K. Wang, J. Jiang, X. Yao, *J. Mater. Chem. A* **2018**, *6*, 8349.
[13] S. Wang, L.-H. Deng, Y.-F. Du, X.-L. Song, *Fuel* **2022**, *315*, 123227.
[14] S. Baranton, C. Coutanceau, C. Roux, F. Hahn, J. M. Léger, *J. Electroanal. Chem.* **2005**, *577*, 223.
[15] M. F. Craciun, S. Rogge, A. F. Morpurgo, *J. Am. Chem. Soc.* **2005**, *127*, 12210.
[16] S. Yang, Y. Yu, X. Gao, Z. Zhang, F. Wang, *Chem. Soc. Rev.* **2021**, *50*, 12985.
[17] D. Liu, Y.-T. Long, *ACS Appl. Mater. Interfaces* **2015**, *7*, 24063.
[18] N. Komba, G. Zhang, Q. Wei, X. Yang, J. Prakash, R. Chenitz, F. Rosei, S. Sun, *Int. J. Hydrogen Energy* **2019**, *44*, 18103.
[19] W. Zhu, F. Xia, Y. Niu, X. Liang, *New J. Chem.* **2020**, *44*, 21108.
[20] A. Arul, H. Pak, K. U. Moon, M. Christy, M. Y. Oh, K. S. Nahm, *Appl Catal B* **2018**, *220*, 488.
[21] C. He, Z.-Y. Wu, L. Zhao, M. Ming, Y. Zhang, Y. Yi, J.-S. Hu, *ACS Catal.* **2019**, *9*, 7311.
[22] N. Safari, P. R. Jamaat, S. A. Shirvan, S. Shoghpour, A. Ebadi, M. Darvishi, A. Shaabani, J. Porphyr, *Phthalocyanines* **2005**, *9*, 256.
[23] K. Sakamoto, E. Ohno-Okumura, *Materials* **2009**, *2*, 1127.
[24] J. H. Zagal, S. Griveau, J. F. Silva, T. Nyokong, F. Bedioui, *Coord. Chem. Rev.* **2010**, *254*, 2755.
[25] N. Kobayashi, *Dimers. Coord. Chem. Rev.* **2002**, *227*, 129.
[26] H. Lu, N. Kobayashi, *Chem. Rev.* **2016**, *116*, 6184.
[27] T. Nyokong, J. Porphyr, *Phthalocyanines* **2020**, *24*, 1300.
[28] A. Koca, A. Kalkan, Z. A. Bayır, *Electrochim. Acta* **2011**, *56*, 5513.
[29] Ö. Bekaroğlu, *Funct. Phthalocyanine Mol. Mater* **2010**, *135*, 105.
[30] A. Sukhikh, D. Bonegardt, D. Klyamer, T. Basova, *Dyes Pigments* **2021**, *192*, 109442.
[31] O. A. Melville, B. H. Lessard, T. P. Bender, *ACS Appl. Mater. Interfaces* **2015**, *7*, 13105.
[32] M. Musilová, J. Mrha, J. Jindra, *J. Appl. Electrochem.* **1973**, *3*, 213.
[33] R. Jasinski, *Nature* **1964**, *201*, 1212.
[34] A. L. Thomas, *Phthalocyanine Research and Applications*, CRC Press, Florida **1990**.
[35] T. Nyokong, *Coord. Chem. Rev.* **2007**, *251*, 1707.
[36] C. Z. Loyola, G. Abarca, S. Ureta-Zañartu, C. Aliaga, J. H. Zagal, M. T. Sougrati, F. Jaouen, W. Orellana, F. Tasca, *J. Mater. Chem. A* **2021**, *9*, 23802.
[37] F. H. Moser, A. L. Thomas, *The phthalocyanines*, CRC Press, Boca Raton **1983**.
[38] Y. S. Korostei, V. G. Tarasova, V. E. Pushkarev, N. E. Borisova, A. K. Vorobiev, L. G. Tomilova, *Dyes Pigments* **2018**, *159*, 573.
[39] T. Jiang, C. Ou, L. Wang, J. Chen, S. Dmytro, Q. Zhang, J. Luo, H. Wang, *J. Rare Earths* **2022**, DOI: https://doi.org/10.1016/j.jre.2022.12.005
[40] N. B. Mckeown, *Phthalocyanine materials: Synthesis, structure and function, an introduction to the phthalocyanine*, Cambridge University Press, Cambridge **1998**.
[41] S. C. Mathur, J. Singh, *Int. J. Quantum Chem.* **1972**, *6*, 57.
[42] B. Ortiz, *J. Electrochem. Soc.* **1996**, *143*, 1800.
[43] H. A. R. Aliabad, M. Bashi, *J. Mater. Sci. Mater. Electron.* **2019**, *30*, 18720.
[44] J. Chen, K. Zou, P. Ding, J. Deng, C. Zha, Y. Hu, X. Zhao, J. Wu, J. Fan, Y. Li, *Adv. Mater.* **2019**, *31*, 1805484.
[45] H. Wu, M. Zeng, X. Zhu, C. Tian, B. Mei, Y. Song, X.-L. Du, Z. Jiang, L. He, C. Xia, S. Dai, *ChemElectroChem* **2018**, *5*, 2717.
[46] R. Matheu, E. Gutierrez-Puebla, M. Á. Monge, C. S. Diercks, J. Kang, M. S. Prevot, X. Pei, N. Hanikel, B. Zhang, P. Yang, O. M. Yaghi, *J. Am. Chem. Soc.* **2019**, *141*, 17081.
[47] B. Ortiz, S. M. Park, N. Doddapaneni, *J. Electrochem. Soc.* **1800**, *1996*, 143.
[48] C. G. Claessens, U. Hahn, T. Torres, *Chem. Rec.* **2008**, *8*, 75.
[49] Z. Liu, C. Liu, Z. Chen, H. Huang, Y. Liu, L. Xue, J. Sun, X. Wang, P. Xiong, J. Zhu, *Exp. Dermatol.* **2023**, *3*, 20220061.
[50] Z. W. Seh, J. Kibsgaard, C. F. Dickens, I. Chorkendorff, J. K. Nørskov, T. F. Jaramillo, *Science* **2017**, *355*, eaad4998.
[51] N. Farajzadeh, D. Akyüz, A. Koca, M. B. Koçak, *Monatsh. Chem.* **2020**, *151*, 1337.
[52] J. Wei, X. Li, C. Xiao, F. Lu, *Vib. Spectrosc.* **2017**, *92*, 105.
[53] G. Z. Anuj Kumar, *J. Electroanal. Chem.* **2022**, *922*, 116799.
[54] H. Li, X. Han, S. Jiang, L. Zhang, W. Ma, R. Ma, Z. Zhou, *Green Energy Environ.* **2022**, *7*, 314.
[55] K. Greulich, A. Belser, S. Bölke, P. Grüninger, R. Karstens, M. S. Sättele, R. Ovsyannikov, E. Giangrisostomi, T. V. Basova, D. Klyamer, T. Chassé, H. Peisert, *J. Phys. Chem. C* **2020**, *124*, 16990.
[56] Z. Zhang, M. Dou, J. Ji, F. Wang, *Nano Energy* **2017**, *34*, 338.
[57] Y. Li, R. Zhang, Y. Cheng, H. Tang, *Mater. Today Sustain.* **2022**, *20*, 100249.
[58] Y. Jiang, Y. Lu, X. Lv, D. Han, Q. Zhang, L. Niu, W. Chen, *ACS Catal.* **2013**, *3*, 1263.
[59] K. Irisa, K. Hatakeyama, S. Yoshimoto, M. Koinuma, S. Ida, *RSC Adv.* **2021**, *11*, 15927.
[60] J. Choi, P. Wagner, S. Gambhir, R. Jalili, D. R. MacFarlane, G. G. Wallace, D. L. Officer, *ACS Energy Lett.* **2019**, *4*, 666.
[61] J. Li, Y. Tang, H. Wang, C. Wang, J. Tian, D. Liu, C. M. Li, C. Guo, *Int. J. Hydrogen Energy* **2022**, *47*, 9905.
[62] I. S. Kwon, I. H. Kwak, J. Y. Kim, H. G. Abbas, T. T. Debela, J. Seo, M. K. Cho, J. P. Ahn, J. Park, H. S. Kang, *Nanoscale* **2019**, *11*, 14266.
[63] X. Zhang, R. Lin, X. Meng, W. Li, F. Chen, J. Hou, *Inorg. Chem.* **2021**, *60*, 9987.
[64] G. Galeotti, F. De Marchi, E. Hamzehpoor, O. MacLean, M. Rajeswara Rao, Y. Chen, L. V. Besteiro, D. Dettmann, L. Ferrari, F. Frezza, P. M. Sheverdyaeva, R. Liu, A. K. Kundu, P. Moras, M. Ebrahimi, M. C. Gallagher, F. Rosei, D. F. Perepichka, G. Contini, *Nat. Mater.* **2020**, *19*, 874.
[65] N. B. McKeown, *J. Mater. Chem.* **2000**, *10*, 1979.
[66] H. Lyu, C. S. Diercks, C. Zhu, O. M. Yaghi, *J. Am. Chem. Soc.* **2019**, *141*, 6848.
[67] R.-R. Liang, S.-Y. Jiang, A. Ru-Han, X. Zhao, *Chem. Soc. Rev.* **2020**, *49*, 3920.

[68] M. Wang, M. Ballabio, M. Wang, H.-H. Lin, B. P. Biswal, X. Han, S. Paasch, E. Brunner, P. Liu, M. Chen, M. Bonn, T. Heine, S. Zhou, E. Cánovas, R. Dong, X. Feng, *J. Am. Chem. Soc.* **2019**, *141*, 16810.
[69] J. Wang, N. Li, Y. Xu, H. Pang, *Chem. A Eur. J.* **2020**, *26*, 6402.
[70] O. M. Yaghi, M. O'Keeffe, N. W. Ockwig, H. K. Chae, M. Eddaoudi, J. Kim, *Nature* **2003**, *423*, 705.
[71] R. Zhou, Y. Huang, Z. Li, S. Kang, X. Wang, S. Liu, *Energy Stor. Mater.* **2021**, *40*, 124.
[72] Y. Yue, P. Cai, K. Xu, H. Li, H. Chen, H. C. Zhou, N. Huang, *J. Am. Chem. Soc.* **2021**, *143*, 18052.
[73] M. Zhao, Y. Huang, Y. Peng, Z. Huang, Q. Ma, H. Zhang, *Chem. Soc. Rev.* **2018**, *47*, 6267.
[74] Y. Li, W. Chen, G. Xing, D. Jiang, L. Chen, *Chem. Soc. Rev.* **2020**, *49*, 2852.
[75] M. Wang, H. Shi, P. Zhang, Z. Liao, M. Wang, H. Zhong, F. Schwotzer, A. S. Nia, E. Zschech, S. Zhou, S. Kaskel, R. Dong, X. Feng, *Adv. Funct. Mater.* **2020**, *30*, 2002664.
[76] S. Yang, Y. Yu, M. Dou, Z. Zhang, F. Wang, *J. Am. Chem. Soc.* **2020**, *142*, 17524.
[77] W. Liu, C. Wang, L. Zhang, H. Pan, W. Liu, J. Chen, D. Yang, Y. Xiang, K. Wang, J. Jiang, X. Yao, *J. Mater. Chem. A* **2019**, *7*, 3112.
[78] Y. Tao, W. Ji, X. Ding, B.-H. Han, *J. Mater. Chem. A* **2021**, *9*, 7336.
[79] D. Rodríguez-San-Miguel, C. Montoro, F. Zamora, *Chem. Soc. Rev.* **2020**, *49*, 2291.
[80] J. D. Yi, D. H. Si, R. Xie, Q. Yin, M. D. Zhang, Q. Wu, G. L. Chai, Y.-B. Huang, *Angew. Chem. Int. Ed.* **2021**, *60*, 17108.
[81] K. Selvaraju, G. A. Babu, *Ionics (Kiel)* **2019**, *25*, 5939.
[82] J. Ge, J. Y. Zheng, J. Zhang, S. Jiang, L. Zhang, H. Wan, L. Wang, W. Ma, Z. Zhou, R. Ma, *J. Mater. Chem. A* **2021**, *9*, 14432.
[83] Z. Wang, J. Zhu, S. Xu, Y. Zhang, B. Van der Bruggen, *J. Membr. Sci.* **2021**, *663*, 119397.
[84] S. Fukuzumi, Y.-M. Lee, *ChemSusChem* **2017**, *10*, 4264.
[85] E. Proietti, F. Jaouen, M. Lefèvre, N. Larouche, J. Tian, J. Herranz, J.-P. Dodelet, *Nat. Commun.* **2011**, *2*, 416.
[86] A. Friedman, M. Mizrahi, N. Levy, N. Zion, M. Zachman, L. Elbaz, *ACS Appl. Mater. Interfaces* **2021**, *13*, 58532.
[87] M. T. M. Koper, *Chem. Sci.* **2013**, *4*, 2710.
[88] X. Ge, A. Sumboja, D. Wuu, T. An, B. Li, F. W. T. Goh, T. S. A. Hor, Y. Zong, Z. Liu, *ACS Catal.* **2015**, *5*, 4643.
[89] S. Sun, N. Jiang, D. Xia, *J. Phys. Chem. C* **2011**, *115*, 9511.
[90] J. Wang, H. Kong, J. Zhang, Y. Hao, Z. Shao, F. Ciucci, *Prog. Mater. Sci.* **2021**, *116*, 100717.
[91] A. Liu, W. Guan, K. Wu, X. Ren, L. Gao, T. Ma, *Appl. Surf. Sci.* **2021**, *540*, 148319.
[92] S. Yuan, J. Peng, Y. Zhang, D. J. Zheng, S. Bagi, T. Wang, Y. Román-Leshkov, Y. Shao-Horn, *ACS Catal.* **2022**, *12*, 7278.
[93] M. L. Pegis, C. F. Wise, D. J. Martin, J. M. Mayer, *Chem. Rev.* **2018**, *118*, 2340.
[94] J. H. Zagal, M. T. M. Koper, *Angew. Chem. Int. Ed.* **2016**, *55*, 14510.
[95] C. Wang, L. Ma, L. Liao, S. Bai, R. Long, M. Zuo, Y. Xiong, *Sci. Rep.* **2013**, *3*, 2580.
[96] Z. Zhang, S. Yang, M. Dou, H. Liu, L. Gu, F. Wang, *RSC Adv.* **2016**, *6*, 67049.
[97] C. Aleksei, S. Chengyi, T. Peng, S. Wen, D. Tao, W. Jianbo, *Prog. Nat. Sci.* **2020**, *30*, 289.
[98] M. H. Seo, D. Higgins, G. Jiang, S. M. Choi, B. Han, Z. Chen, *J. Mater. Chem. A* **2014**, *2*, 19707.
[99] L. Li, X. Tang, S. Huang, C. Lu, D. Lützenkirchen-Hecht, K. Yuan, X. Zhuang, Y. Chen, *Angew. Chem. Int. Ed.* **2023**, *62*, e202301642.
[100] Y. Hong, L. Li, B. Huang, X. Tang, W. Zhai, T. Hu, K. Yuan, Y. Chen, *Adv. Energy Mater.* **2021**, *11*, 2100866.
[101] X. Zhong, L. Liu, X. Wang, H. Yu, G. Zhuang, D. Mei, X. Li, J.-G. Wang, *J. Mater. Chem. A* **2014**, *2*, 6703.
[102] K. Chen, K. Liu, P. An, H. Li, Y. Lin, J. Hu, C. Jia, J. Fu, H. Li, H. Liu, Z. Lin, W. Li, J. Li, Y.-R. Lu, T.-S. Chan, N. Zhang, M. Liu, *Nat. Commun.* **2020**, *11*, 4173.
[103] H. Zhong, K. H. Ly, M. Wang, Y. Krupskaya, X. Han, J. Zhang, J. Zhang, V. Kataev, B. Buchner, I. M. Weidinger, S. Kaskel, P. Liu, M. Chen, R. Dong, X. Feng, *Angew. Chem. Int. Ed.* **2019**, *58*, 10677.
[104] K. M. Zhao, S. Liu, Y. Y. Li, X. Wei, G. Ye, W. Zhu, Y. Su, J. Wang, H. Liu, Z. He, Z. Y. Zhou, S. G. Sun, *Adv. Energy Mater.* **2022**, *12*, 2103588.
[105] W.-Z. Cheng, J.-L. Liang, H.-B. Yin, Y.-J. Wang, W.-F. Yan, J.-N. Zhang, *Rare Metals* **2020**, *39*, 815.
[106] C. Sun, Z. Li, J. Yang, S. Wang, X. Zhong, L. Wang, *Catal. Today* **2020**, *353*, 279.
[107] L. Lv, Z. Yang, K. Chen, C. Wang, Y. Xiong, *Adv. Energy Mater.* **2019**, *9*, 1803358.
[108] S. Yang, Y. Yu, M. Dou, Z. Zhang, L. Dai, F. Wang, *Angew. Chem. Int. Ed.* **2019**, *58*, 14724.
[109] Z.-F. Huang, J. Wang, Y. Peng, C.-Y. Jung, A. Fisher, X. Wang, *Adv. Energy Mater.* **2017**, *7*, 1700544.
[110] P. Gono, A. Pasquarello, *J. Chem. Phys.* **2020**, *152*, 104712.
[111] W. T. Hong, M. Risch, K. A. Stoerzinger, A. Grimaud, J. Suntivich, Y. Shao-Horn, *Energ. Environ. Sci.* **2015**, *8*, 1404.
[112] J. Zhang, H. B. Yang, D. Zhou, B. Liu, *Chem. Rev.* **2022**, *122*, 17028.
[113] A. Papaderakis, D. Tsiplakides, S. Balomenou, S. Sotiropoulos, *J. Electroanal. Chem.* **2015**, *757*, 216.
[114] X. Zhang, X. Li, W. Wang, Z. Yang, *Surf. Sci.* **2022**, *717*, 122000.
[115] S. Aralekallu, V. A. Sajjan, M. Palanna, C. P. Prabhu, M. Hojamberdiev, L. K. Sannegowda, *J. Power Sources* **2020**, *449*, 227516.
[116] C. Li, T. Huang, Z. Huang, J. Sun, C. Zong, J. Yang, W. Deng, F. Dai, *Dalton Trans.* **2019**, *48*, 17258.
[117] H. Jia, Y. Yao, J. Zhao, Y. Gao, Z. Luo, P. Du, *J. Mater. Chem. A* **2018**, *6*, 1188.
[118] D. Qi, X. Chen, W. Liu, C. Liu, W. Liu, K. Wang, J. Jiang, *Inorg. Chem. Front.* **2020**, *7*, 642.
[119] Y. Zang, D. Q. Lu, K. Wang, B. Li, P. Peng, Y. Q. Lan, S. Q. Zang, *Nat. Commun.* **2023**, *14*, 1792.
[120] J. Li, P. Liu, J. Mao, J. Yan, W. Song, *J. Mater. Chem. A* **2021**, *9*, 1623.
[121] J. Li, P. Liu, J. Mao, J. Yan, W. Song, *J. Mater. Chem. A* **2021**, *9*, 11248.
[122] Y. Shi, B. Zhang, *Chem. Soc. Rev.* **2016**, *45*, 1781.
[123] S. Chu, A. Majumdar, *Nature* **2012**, *488*, 294.
[124] Y. Jiao, Y. Zheng, M. Jaroniec, S. Z. Qiao, *Chem. Soc. Rev.* **2015**, *44*, 2060.
[125] A. Wang, C. Li, J. Zhang, X. Chen, L. Cheng, W. Zhu, *J. Colloid Interface Sci.* **2019**, *556*, 159.
[126] G. R. Monama, S. B. Mdluli, G. Mashao, M. D. Makhafola, K. E. Ramohlola, K. M. Molapo, M. J. Hato, K. Makgopa, E. I. Iwuoha, K. D. Modibane, *Renew. Energy* **2018**, *119*, 62.
[127] J. Safaei, P. Xiong, G. Wang, *Mater. Today Adv.* **2020**, *8*, 100108.
[128] L. Sun, V. Reddu, A. C. Fisher, X. Wang, *Energ. Environ. Sci.* **2020**, *13*, 374.
[129] C. Costentin, M. Robert, J. Savéant, *Chem. Soc. Rev.* **2013**, *42*, 2423.
[130] Z. Yue, C. Ou, N. Ding, L. Tao, J. Zhao, J. Chen, *ChemCatChem* **2020**, *12*, 6103.
[131] J. T. Feaster, C. Shi, E. R. Cave, T. Hatsukade, D. N. Abram, K. P. Kuhl, C. Hahn, J. K. Nørskov, T. F. Jaramillo, *ACS Catal.* **2017**, *7*, 4822.
[132] J. Qiao, Y. Liu, F. Hong, J. Zhang, *Chem. Soc. Rev.* **2014**, *43*, 631.
[133] J.-J. Ma, H.-L. Zhu, Y.-Q. Zheng, M. Shui, *ACS Appl. Energy Mater.* **2021**, *4*, 1442.
[134] Y. Y. Birdja, E. Pérez-Gallent, M. C. Figueiredo, A. J. Göttle, F. Calle-Vallejo, M. T. M. Koper, *Nat. Energy* **2019**, *4*, 732.
[135] H. A. Hansen, J. B. Varley, A. A. Peterson, J. K. Nørskov, *J. Phys. Chem. Lett.* **2013**, *4*, 388.
[136] D. L. T. Nguyen, Y. Kim, Y. J. Hwang, D. H. Won, *Carbon Energy* **2020**, *2*, 72.

[137] X. Yang, J. Cheng, X. Xuan, N. Liu, J. Liu, *ACS Sustain. Chem. Eng.* **2020**, *8*, 10536.
[138] X. Wang, Y. Fu, D. Tranca, K. Jiang, J. Zhu, J. Zhang, S. Han, C. Ke, C. Lu, X. Zhuang, *ACS Appl. Energy Mater.* **2021**, *4*, 2891.
[139] J. Wang, X. Huang, S. Xi, J.-M. Lee, C. Wang, Y. Du, X. Wang, *Angew. Chem. Int. Ed.* **2019**, *58*, 13532.
[140] C. L. Yao, J. C. Li, W. Gao, Q. Jiang, *Chem. A Eur. J.* **2018**, *24*, 11051.
[141] N. Huang, K. H. Lee, Y. Yue, X. Xu, S. Irle, Q. Jiang, D. Jiang, *Angew. Chem. Int. Ed.* **2020**, *59*, 16587.
[142] M. Lu, M. Zhang, C. G. Liu, J. Liu, L. J. Shang, M. Wang, J. N. Chang, S. L. Li, Y. Q. Lan, *Angew. Chem. Int. Ed.* **2021**, *60*, 4864.
[143] M. D. Zhang, D. H. Si, J. D. Yi, S. S. Zhao, Y. B. Huang, R. Cao, *Small* **2020**, *16*, 2005254.
[144] B. Han, X. Ding, B. Yu, H. Wu, W. Zhou, W. Liu, C. Wei, B. Chen, D. Qi, H. Wang, K. Wang, Y. Chen, B. Chen, J. Jiang, *J. Am. Chem. Soc.* **2021**, *143*, 7104.
[145] Z. Weng, Y. Wu, M. Wang, J. Jiang, K. Yang, S. Huo, X. F. Wang, Q. Ma, G. W. Brudvig, V. S. Batista, Y. Liang, Z. Feng, H. Wang, *Nat. Commun.* **2018**, *9*, 415.
[146] X.-F. Qiu, H.-L. Zhu, J.-R. Huang, P.-Q. Liao, X.-M. Chen, *J. Am. Chem. Soc.* **2021**, *143*, 7242.
[147] X. F. Qiu, J. R. Huang, C. Yu, Z. H. Zhao, H. L. Zhu, Z. Ke, P. Q. Liao, X. M. Chen, *Angew. Chem. Int. Ed.* **2022**, *61*, e202206470.
[148] S. L. Foster, S. I. P. Bakovic, R. D. Duda, S. Maheshwari, R. D. Milton, S. D. Minteer, M. J. Janik, J. N. Renner, L. F. Greenlee, *Nat. Catal.* **2018**, *1*, 490.
[149] S. Giddey, S. P. S. Badwal, A. Kulkarni, *Int. J. Hydrogen Energy* **2013**, *38*, 14576.
[150] E. Skúlason, T. Bligaard, S. Gudmundsdóttir, F. Studt, J. Rossmeisl, F. Abild-Pedersen, T. Vegge, H. Jónsson, J. K. Nørskov, *Phys. Chem. Chem. Phys.* **2012**, *14*, 1235.
[151] X. Guo, J. Gu, S. Lin, S. Zhang, Z. Chen, S. Huang, *J. Am. Chem. Soc.* **2020**, *142*, 5709.
[152] H. Liu, *Chin. J. Catal.* **2014**, *35*, 1619.
[153] Y. Abghoui, E. Skúlasson, *Proc. Comp. Sci.* **2015**, *5*, 1897.
[154] N. Morlanés, W. Almaksoud, R. K. Rai, S. Ould-Chikh, M. M. Ali, B. Vidjayacoumar, B. E. Al-Sabban, K. Albahily, J.-M. Basset, *Cat. Sci. Technol.* **2020**, *10*, 844.
[155] T. Xu, B. Ma, J. Liang, L. Yue, X. Sun, *Recent Acta Phys. Chim. Sin.* **2021**, *37*, 2009043.
[156] S. Murmu, S. Paul, A. Santra, M. Robert, U. K. Ghorai, *Catal. Today* **2022**, *423*, 113938.
[157] S. Xu, Y. Ding, J. Du, Y. Zhu, G. Liu, Z. Wen, X. Liu, Y. Shi, H. Gao, L. Sun, F. Li, *ACS Catal.* **2022**, *12*, 5502.
[158] M. Jiang, L. Han, P. Peng, Y. Hu, Y. Xiong, C. Mi, Z. Tie, Z. Xiang, Z. Jin, *Nano Lett.* **2022**, *22*, 372.
[159] F. Yao, C. Fang, J. Cui, L. Dai, X. Zhang, L. Xue, P. Xiong, Y. Fu, W. Zhang, J. Sun, J. Zhu, *Natl. Sci. Open* **2023**, *2*, 20220032.
[160] G.-B. Wang, S. Li, C.-X. Yan, F.-C. Zhu, Q.-Q. Lin, K.-H. Xie, Y. Geng, Y.-B. Dong, *J. Mater. Chem. A* **2020**, *8*, 6957.
[161] N. Keller, T. Bein, *Chem. Soc. Rev.* **2021**, *50*, 1813.
[162] H. Yang, D. Yang, Y. Zhou, X. Wang, *J. Am. Chem. Soc.* **2021**, *143*, 13721.
[163] Y. Deng, Y. Wang, X. Xiao, B. J. Saucedo, Z. Zhu, M. Xie, X. Xu, K. Yao, Y. Zhai, Z. Zhang, J. Chen, *Small* **2022**, *18*, 2202928.
[164] P. Xiong, Y. Wu, Y. Liu, R. Ma, T. Sasaki, X. Wang, J. Zhu, *Energ. Environ. Sci.* **2020**, *13*, 4834.
[165] X. Huang, C. Sun, X. Feng, *Sci. China Chem.* **2020**, *63*, 1367.